

Magnetized Chitosan Nanocomposite as an Effective Adsorbent for the Removal of Methylene Blue and Malachite Green Dyes

Fouzia Mashkoor

Aligarh Muslim University Faculty of Engineering and Technology

Abu Nasar (✉ abunasaramu@gmail.com)

Aligarh Muslim University <https://orcid.org/0000-0001-8796-3077>

Research Article

Keywords: Adsorption, Dye, Malachite green, Methylene blue, Wastewater treatment, Magnetized chitosan

Posted Date: March 9th, 2021

DOI: <https://doi.org/10.21203/rs.3.rs-233253/v1>

License:  This work is licensed under a Creative Commons Attribution 4.0 International License.

[Read Full License](#)

Version of Record: A version of this preprint was published at Biomass Conversion and Biorefinery on January 4th, 2022. See the published version at <https://doi.org/10.1007/s13399-021-02282-3>.

1 **Magnetized chitosan nanocomposite as an effective adsorbent for the removal of methylene**
2 **blue and malachite green dyes**

3 **Fouzia Mashkoo, Abu Nasar***

4 Department of Applied Chemistry, Faculty of Engineering and Technology, Aligarh Muslim
5 University, Aligarh – 202 002, India

6

7 **Abstract**

8 Herein, a magnetically separable Fe_3O_4 decorated chitosan was facilely synthesized,
9 systematically characterized, and subsequently employed as a versatile adsorbing material for the
10 adsorption of malachite green and methylene blue dyes. The prepared adsorbent was
11 characteristically examined through Fourier transform infra-red microscopy, scanning electron
12 microscopy with energy-dispersive X-ray analysis, transmission electron microscopy X-ray
13 diffraction, Brunauere-Emmette-Teller surface area analysis, thermogravimetric analysis, and
14 vibrating-sample magnetometry techniques. The performance of adsorbent was studied in batch
15 mode and the the time-dependent experimental data were analyzed with different kinetic models,
16 and pseudo-IInd-order was provided the best fit for the adsorption of both the dyes with a high
17 value of the regression coefficient. The adsorption equilibrium data of both the dyes was best
18 explained by Langmuir isotherm, and the maximum sorption capacity of MG and MB was found
19 to be 55.86 and 76.34 mg g^{-1} , respectively. Thermodynamic analysis declared that the adsorption
20 of MG and MB onto the MChi was endothermic and spontaneous in nature. Moreover, the
21 adsorbent presented good reusability up to three successive ad-/de-sorption cycles, indicating
22 that MChi is a promising applicant for the treatment of dye-containing wastewater.

23

24 *Corresponding author. E-mail address: abunasar@zhcet.ac.in, abunasaramu@gmail.com (A.
25 Nasar)

26

27 Keywords: Adsorption; Dye; Malachite green; Methylene blue; Wastewater treatment;
28 Magnetized chitosan

29

30 **Introduction**

31 Water lack is one of the most severe worries that our world is confronting nowadays (Franco et
32 al. 2019). By 2050, over 40% of the world population is expected to live in regions of extreme
33 water scarcity (Novais et al. 2018). The inexorable decline in the quality and availability of
34 drinking water is undoubtedly the consequence of the increasing growth of the world population
35 and unsustainable industrial development. Water is polluted by the inevitable discharge of
36 industrial wastewater comprising numerous non-biodegradable and hazardous inorganic and
37 organic contaminants like heavy metals, pesticides, dyes, cosmetics, and pharmaceuticals, etc.
38 (Lehman et al. 2011; Kant 2012; Zhao et al. 2013, 2015; Tomar et al. 2014; Qamruzzaman and
39 Nasar 2015, 2019; Ippolito and Fait 2019; Quesada et al. 2019; Jain et al. 2019, 2020; Agarwal et
40 al. 2020). Among these contaminants, the discharge of dyeing sewage from various industries
41 have triggered visual severe water pollution and reduces the water transparency due to extremely
42 high color strength, and leading to a corresponding rise in the concentration of organic matter in
43 water bodies. In addition, it restrains the photosynthesis activity and ends up interfering with

44 aquatic biological processes and imparting enduring potential harm to the ecosphere and humans
45 as well (Jafari et al. 2015; Shakoor and Nasar 2016; Nasar and Mashkooor 2019; Kang et al.
46 2020). Hence, from the viewpoint of environmental safeguard, it is an extremely imperative
47 prerequisite to developing high performance and eco-friendly technology to eliminate or
48 minimize the content of dyes present in industrial sewage before releasing into the receiving
49 water system. Nowadays, the techniques for the treatment of dyes-laden effluent include
50 photocatalytic degradation, electrochemical treatment, biological method, membrane separation,
51 adsorption, and so on.

52 Nevertheless, while these methods described above have many constrictions, compared to
53 them, adsorption has demonstrated to be more efficient as it offers many advantages such as
54 simplicity in design, cost-effective, eco-friendly, and easy to operate (Hokkanen et al. 2016;
55 Shakoor and Nasar 2017; Mashkooor and Nasar 2020a; Mashkooor et al. 2020). Primarily, the
56 contaminant elimination act of the adsorption technique is mainly dependent on the
57 characteristics of the adsorbing material like high porosity and surface area, remarkable
58 adsorption capacity, a large number of exposed functional groups and chemical resistance, etc.
59 Thus, recent studies have shown that many researcher have made outstanding efforts to produce
60 several efficient adsorbents that have been utilized magnificently for the removal of toxic
61 pollutants from wastewater.

62 Natural polymer and its derivatives have possessed remarkable benefits of low cost and
63 abundance and the presence of numerous functional groups in the wastewater application (Lou et
64 al. 2019). For instance, chitosan (Chi) has already been well-known as the most plentiful
65 naturally occurring biopolymers. Chi has captivating characteristics, such as nonhazardous,
66 hydrophilicity, antibacterial property, biodegradability, and biocompatibility (Vakili et al. 2019;

67 Sabar et al. 2020). The presence of hydroxyl and amino groups in its molecular chain has served
68 as favorable binding sites for both cationic and anionic contaminants present in the wastewater
69 (Lou et al. 2019). However, owing to the high solubility of Chi at pH less than 5.5, it is
70 challenging to be separated and recovered by traditional separation techniques, such as high-
71 speed centrifugation and filtration (Fan et al. 2012). Tailoring of Chi with magnetic particles is
72 an efficient way to overcome these limitations since magnetized chitosan possesses the benefits
73 of both chitosan (admirable adsorption efficiency) and magnetic material (easy magnetic
74 separability) (Chen et al. 2019).

75 Here in this report, a stable and magnetically recyclable Chi based bioadsorbent was
76 prepared and explored for the adsorption of two different pollutant dyes, i.e., cationic malachite
77 green (MG), and methylene blue (MB). The adsorption performance of MChi to eliminate the
78 abovementioned dyes were systematically examined at various adsorbate concentrations, MChi
79 dosage, pH of the solution, adsorbate/adsorbent interaction time, and temperature. The rigorous
80 analyses of adsorption data were carried out in the light of popular kinetic and isotherm models.
81 Moreover, the regeneration experiments of exhausted MChi were executed with the inexpensive
82 desorbing materials, which also demonstrated its promising utility in the wastewater
83 management.

84 **Materials and methods**

85 **Materials**

86 Microscopic grade of dyes (MB and MG) other chemicals (anhydrous ferric chloride, ferrous
87 chloride dihydrated, potassium nitrate, glacial acetic acid, sodium hydroxide, and hydrochloric
88 acid) each of analytical reagent grade procured from Central Drug House, India were used. The

89 extra pure chitosan of medium molecular weight obtained from Sisco Research Laboratories,
90 India were used as received.

91 **Preparation of MChi**

92 The MChi was prepared by incorporating Fe₃O₄ particles to Chi by adopting a method similar to
93 our previous work details of was described earlier (Mashkooor and Nasar 2020b).

94

95 **Characterizations**

96 All Characterization and analysis methods are provided in supporting information (Text S1).

97 **Adsorption procedure**

98 The MG and MB adsorption onto the MChi was appraised using batch methods. The dye
99 solution of the desired concentration was obtained by appropriate dilution of a stock solution (1 g
100 L⁻¹). Specifically, MChi adsorbent was transferred into the 30 ml of dye solution, the pH of
101 which was adjusted with 0.1 M NaOH or HCl solutions. After the acquirement of equilibrium,
102 the adsorbate-loaded magsorbent was separated from the solution employing an external
103 magnetic field, and the left over-concentration of dye was analyzed by UV-VIS
104 spectrophotometer (Thermo Scientific, Evolution 201) at λ_{\max} of 617 nm for MG and 665 nm for
105 MB.

106 The adsorption capacity (q) at any moment (t)/equilibrium (e) of MChi and the removal
107 efficiency (RE %) were calculated according to equations 1 and 2, respectively (Mashkooor et al.
108 2018):

109
$$q_{t/e} = \frac{V}{m} \times (C_o - C_{t/e}) \quad (1)$$

110
$$RE\% = \frac{(C_o - C_{t/e})}{C_o} \times 100 \quad (2)$$

111 where C_o and C are the initial and residual dye concentration at any moment/equilibrium (t/e) in
112 mg L^{-1} , respectively. V is the volume of adsorbate solution (L), m is the MChi dosage (g).

113 For the acquisition of the optimal value, the influence of MChi dose ($0.4\text{--}6 \text{ g L}^{-1}$), pH of the dye
114 solution (4–11), contact time (2–240 min), and initial adsorbate concentration ($15\text{--}100 \text{ mg L}^{-1}$)
115 was studied by batch technique. The influence of temperature ($303\text{--}333 \text{ K}$) was also
116 investigated.

117

118 **Desorption and regeneration study of the MChi**

119 The possibility of recycling the MChi was evaluated using 0.1 M HCl and ethanol as a desorbing
120 agent for the desorption of MG and MB from the MChi. The experiments were performed by
121 adding dye saturated adsorbent into the 30 ml of aforementioned desorbing agents at $30 \text{ }^\circ\text{C}$ and
122 left for 4 h for desorption equilibrium. A similar method of ad-/de-sorption cycles was replicated
123 to reappraise the performance of the MChi till the removal of dye become inconsequential. The
124 concentration of dye in the solution after every ad-/de-sorption cycle was determined, and
125 percent desorption (D%) was evaluated using equation 4:

126
$$D\% = \frac{W_{\text{des}}}{W_{\text{ads}}} \times 100 \quad (4)$$

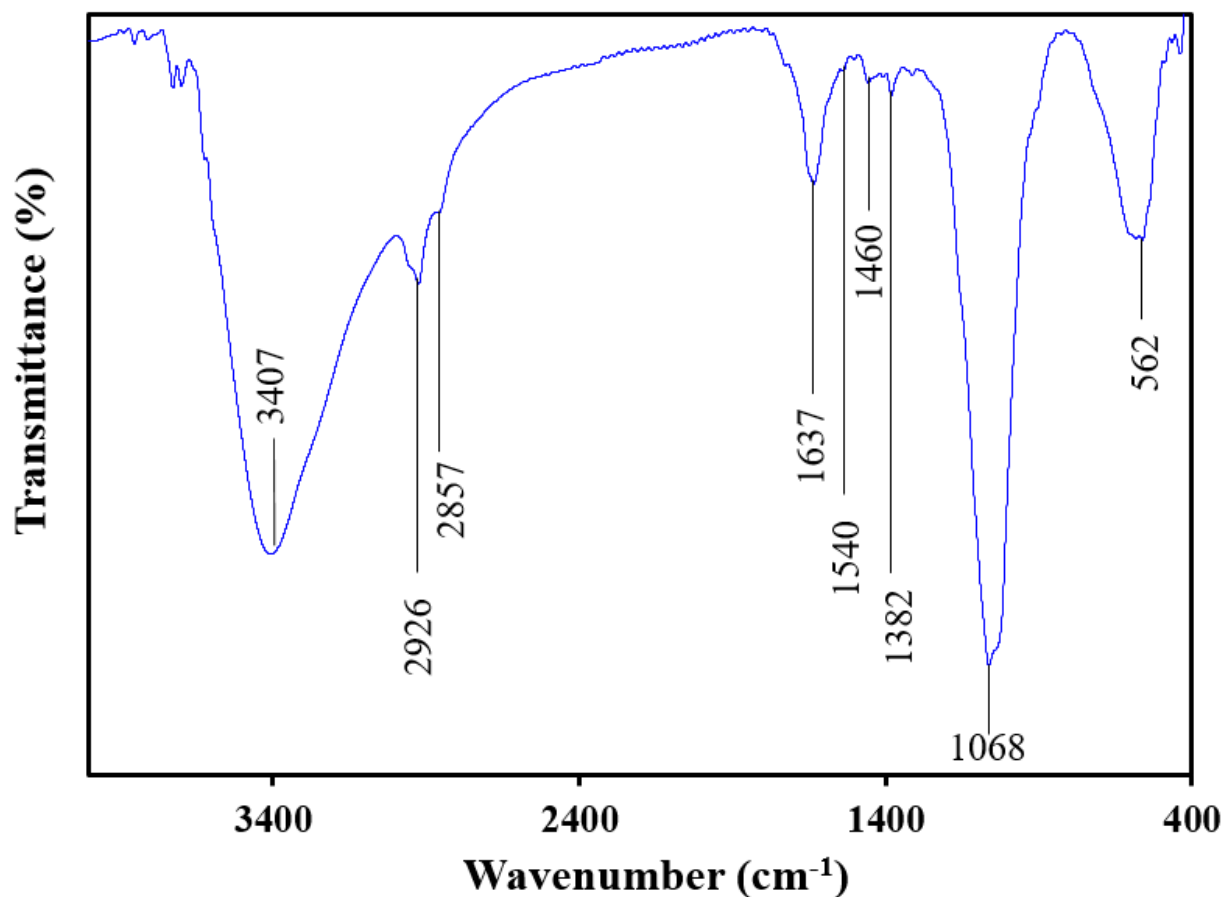
127 where, W_{ads} is the amount dye adsorbed, and W_{des} is the amount of dye desorbed in mg L^{-1} .

128 **Results and discussion**

129 **Adsorbent characterization**

130 The Fourier transform infra-red (FTIR) spectra of MChi illustrated in Fig. 1 was consisted of
131 characteristic peaks at 3407 and 2926 cm^{-1} , attributed to the axial stretching vibrations of O-H
132 and N-H groups (Prasad and Joseph 2017). A small peak near 2857 cm^{-1} was endorsed to the
133 stretching vibrations of C-H, and the band of significant intensity around 1637 cm^{-1} was due to
134 the stretching vibrations of amide I (NH deformation of $-\text{NHCOCH}_3$). Peaks appeared at 1460
135 and 1382 cm^{-1} were attributed to coupling of C-N axial stretching and N-H angular deformation,
136 respectively. The peak at 1068 cm^{-1} was allocated to the C-O-C stretching vibration, and one
137 additional peak at 562 cm^{-1} was due to the stretching vibration of Fe-O (Bagheri et al. 2014).

138

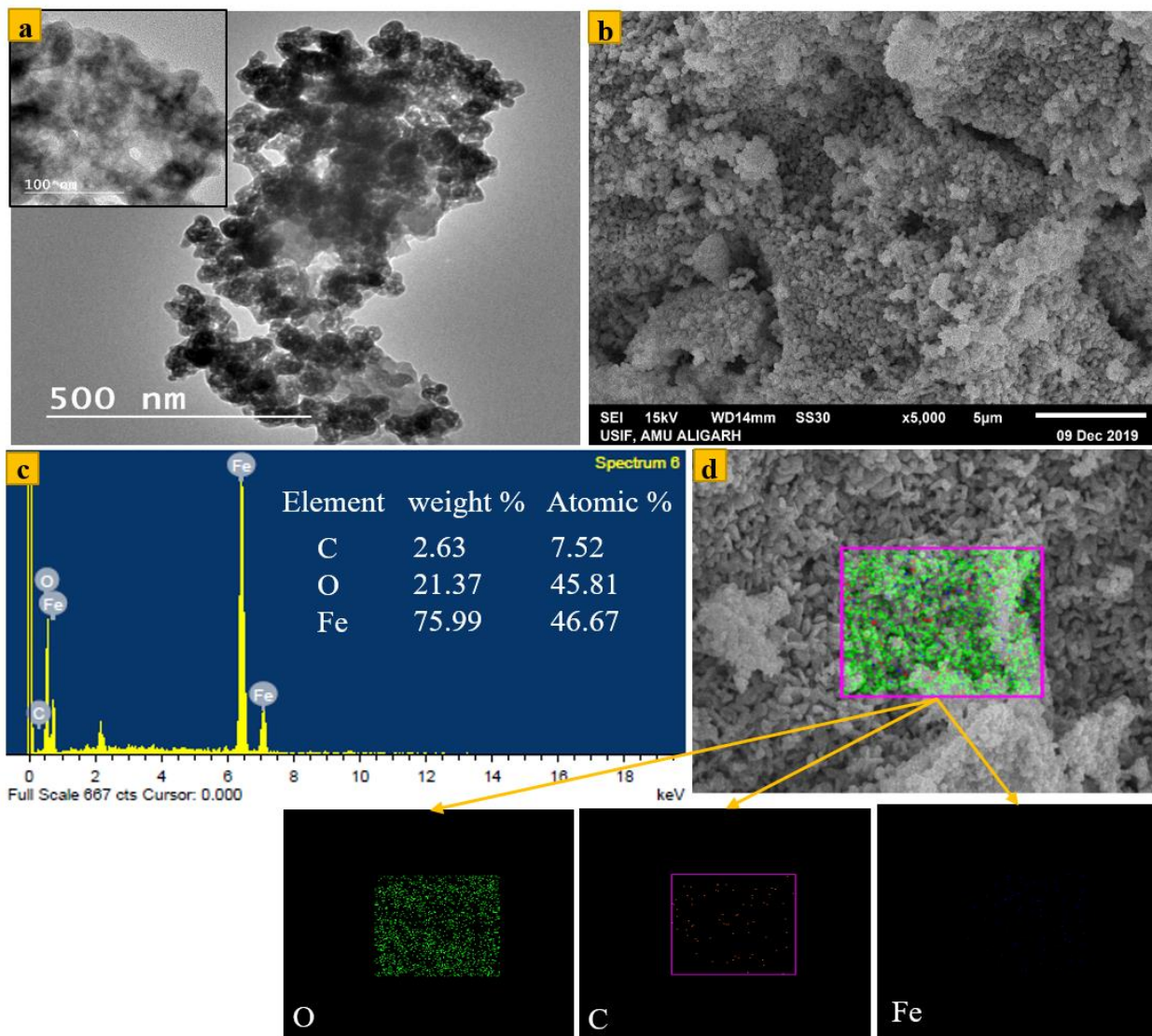


139

140 **Fig. 1** (a) FTIR of MChi

141

142 The morphology of MChi nanocomposite was characterized by transmission electron
 143 microscopy (TEM) and scanning electron microscopy (SEM) observations. The TEM images of
 144 MChi presented in Fig. 2a revealed the smaller and compact nanoparticles which comprise of
 145 dark color ellipsoidal and spherical shaped particles of Fe₃O₄ and the light contrast matrix of Chi.
 146 The SEM image of MChi (Fig. 2b) indicated the agglomerated light color mass of Chi present on
 147 the surface of uniformly distributed particles of Fe₃O₄. The energy-dispersive X-ray analysis
 148 (EDAX) and elemental mapping of the nanoparticles, as shown in Fig. 2c and Fig. 2d,
 149 respectively, ensured the occurrence of C, O and Fe elements in the composite of MChi.



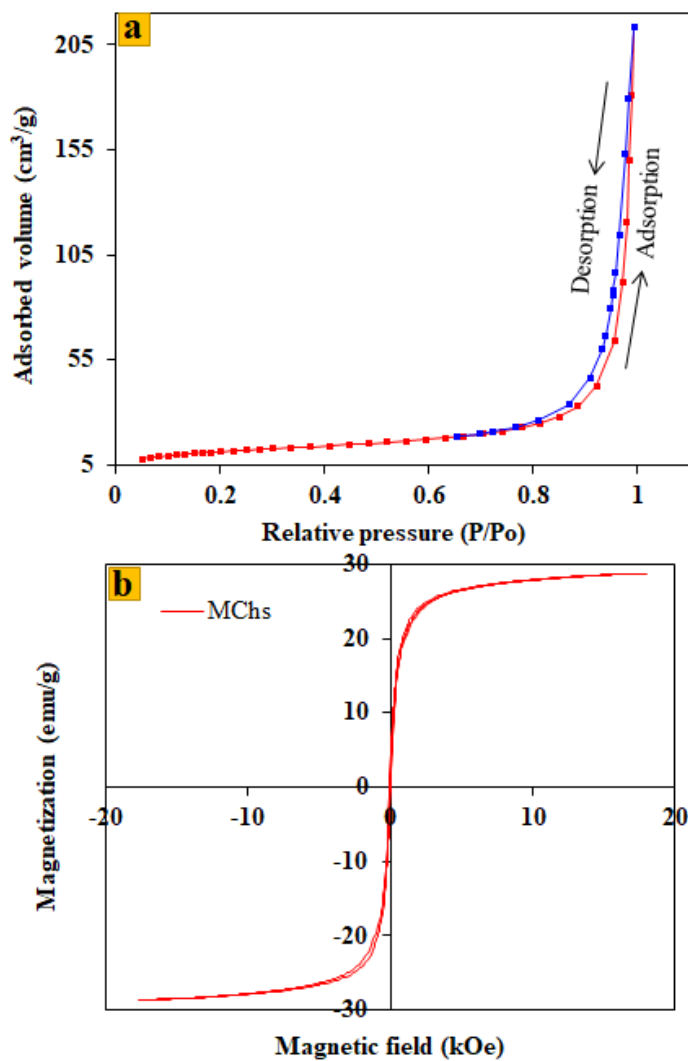
150

151 **Fig. 2** (a) TEM images (b) SEM image (c) EDAX image (d) Elemental mapping of MChi

152 In order to examine the surface area and porosity of the MChi, N₂ ad-/de-sorption
 153 isotherms were enumerated (Fig. 3a). The shape of the curve specified in essence is the type-IV
 154 isotherm according to IUPAC nomenclature with the mesoporous characteristic of the MChi and
 155 is represented in Fig. 3a. Moreover, the interpretation of the hysteresis loop exemplified the
 156 existence of type H3 loop, as outlined in the literature (Qi et al. 2017). The obtained results
 157 indicated that the Brunauere-Emmette-Teller (BET) surface area of MChi was about 39.99 m² g⁻¹

158 ¹. According to the Barrett–Joyner–Halenda (BJH) analyses (Fig. 3a'), the MChi possess the
159 average pore width of 39.9751 nm, which also corresponds to the mesoporous nature of the
160 materials.

161 The magnetic behavior of MChi was studied by vibrating-sample magnetometry (VSM)
162 at room temperature, and the typical magnetic curve and the values of the magnetic properties of
163 MChi are presented in Fig. 3b and b', respectively. The saturation magnetization of MChi was
164 28.645 emu g⁻¹, demonstrating the magnetic nature of the composite, which is sufficient enough
165 for conventional magnetic separation. The respective values of intrinsic coercivity and retentivity
166 determined from VSM for MChi were 54.507 Oe, and 2.9258 emu g⁻¹. The magnetic hysteresis
167 loop of MChi (Fig. 3b) displayed an S-shaped curve with low value of retentivity, which
168 signifies good dispersibility and easy demagnetization. Therefore, MChi may be a worthy
169 candidate for the wastewater remediation and may be efficiently isolated from water by
170 employing a magnetic field (Saravanakumar et al. 2019).



(a') Summary of the BET analysis of MChi

Parameters	Values
Single-point surface area at $P/P_0=0.3001$	38.4813 m ² /g
Single-point adsorption total pore volume of the pores (pores less than 2988.714 Å diameter at $P/P_0=0.993559$)	0.33003 cm ³ /g
BET surface area	39.9930 m ² /g
Adsorption average pore width (4V/A by BET)	33.00897 nm
t-plot external surface area	39.1537 m ² /g
t-plot micropore area	0.8393 m ² /g
t-plot micropore volume	0.000187 cm ³ /g
BJH adsorption cumulative surface area of pores between 17-3000 Å diameter	33.553 m ² /g
BJH adsorption average pore width (4V/A by BET)	38.9751 nm
BJH desorption cumulative surface area of pores between 17-3000 Å diameter	36.7427 m ² /g
BJH desorption average pore width (4V/A by BET)	35.8733 nm

(b') Magnetic properties of MChi

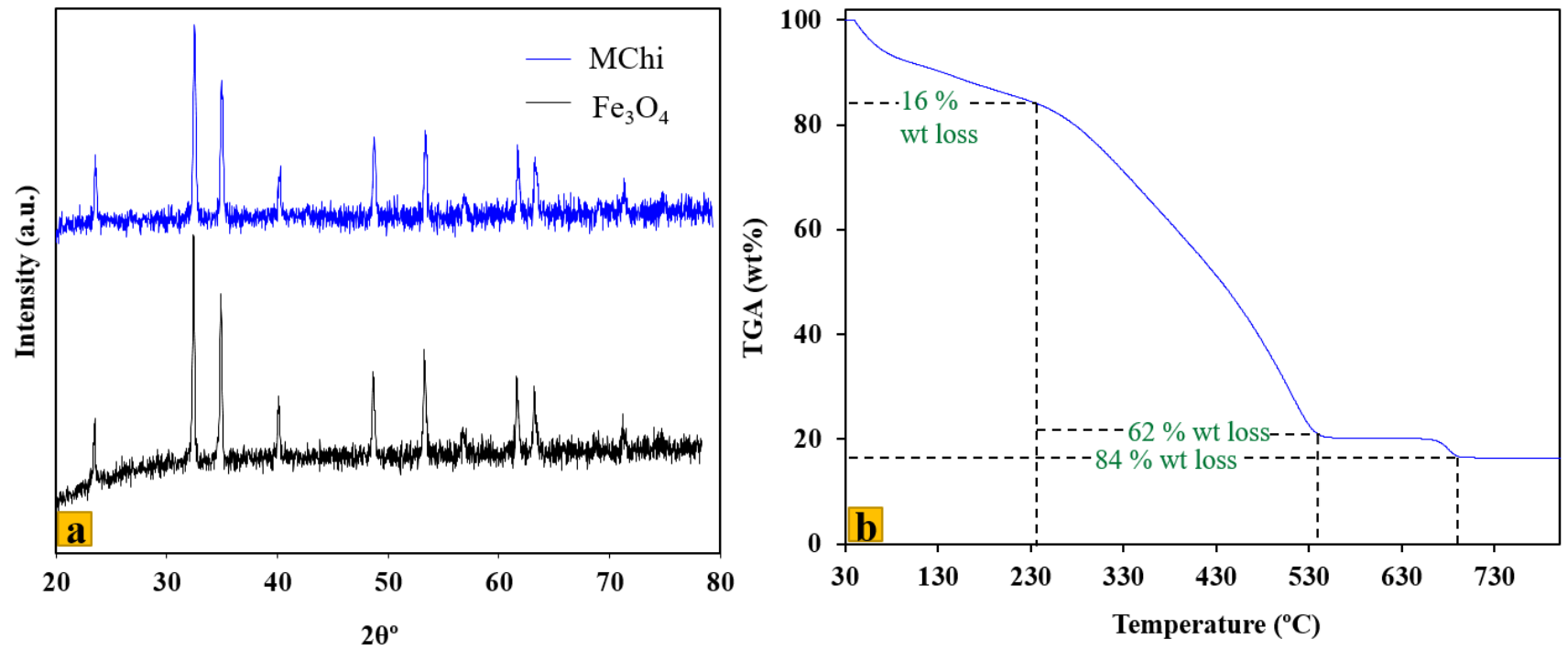
Parameters	Values
Coercivity (Hc)	54.507 Oe
Magnetization (Ms)	28.645 emu/g
Retentivity (M)	2.9258 emu/g

171

172 **Fig. 3** (a) N₂ ad-/de-sorption isotherm, (a') Summary of the BET analyses (b) Magnetization curve (b') Magnetic properties of MChi

173 Fig. 4a shows the X-ray diffraction (XRD) patterns of Fe₃O₄ and MChi. The XRD pattern
174 of Fe₃O₄ shows the peaks at 2θ of 32.42, 34.88, 40.08, 48.63, 53.22, 56.8, 61.63, 63.15 and 71.2
175 which are agreeing with the standard Fe₃O₄ XRD pattern, ascertain that the Fe₃O₄ are inverse
176 cubic spinel structure (Kazeminezhad and Mosivand 2014; Zhu et al. 2017). An almost similar
177 XRD pattern of MChi was noticed, which suggests that the presence of Chi does not change the
178 crystallinity of Fe₃O₄.

179 The thermogravimetric analysis (TGA) plot of MChi illustrated in Fig. 4b presented a
180 weight loss of 16 % below 240 °C, referring to the loss of moisture and thereafter a rapid and
181 major weight loss of about 62 % in between 240–540 °C, accounted for the degeneration of Chi
182 chain and cleavage of the ether linkage in the Chi backbone (Cao et al. 2014; Cabuk et al. 2014).
183 The average mass losses of MChi was estimated to be about 84 % at degradation temperature of
184 700 °C.



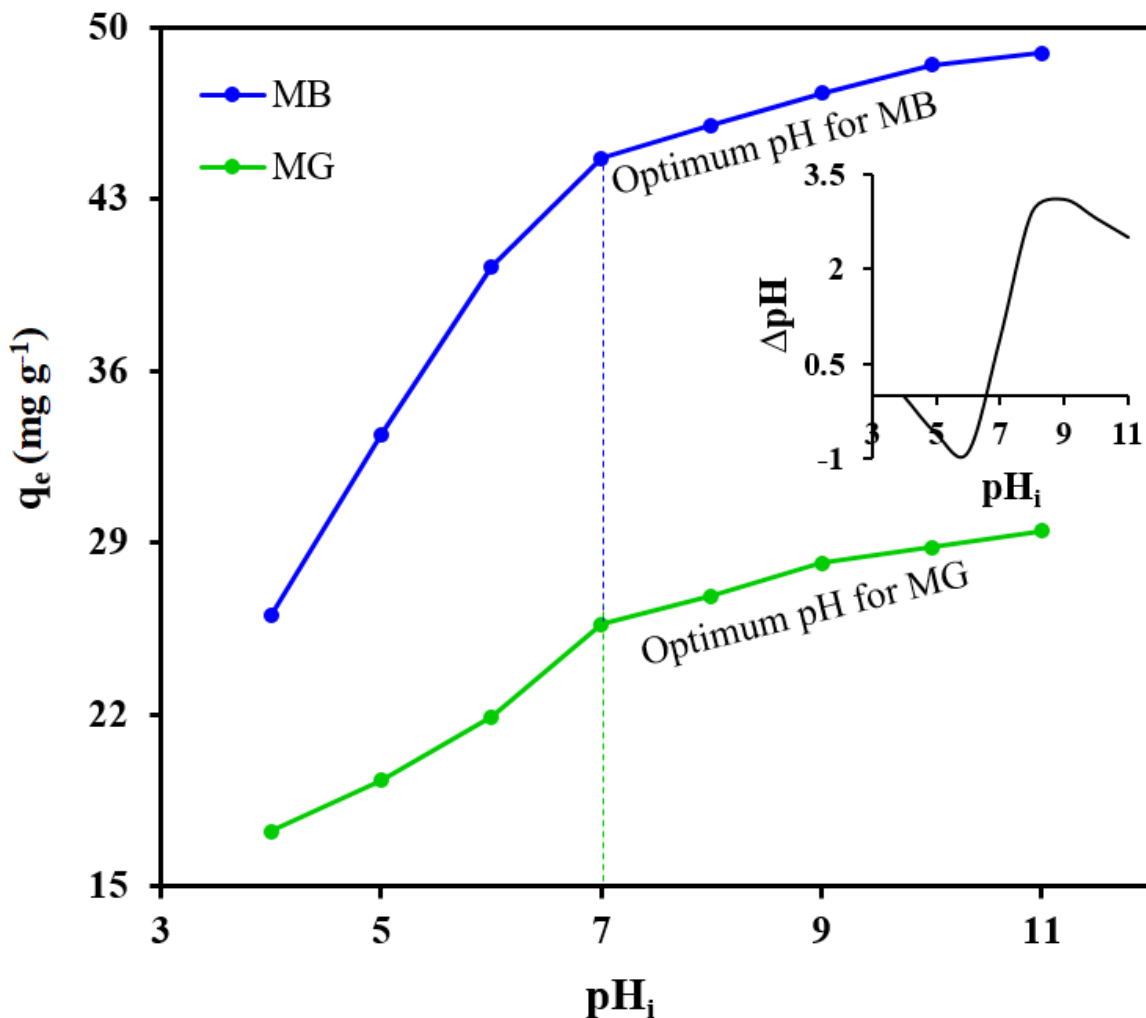
185

186 **Fig. 4** XRD patterns of Fe₃O₄, and MChi (b)TGA plot of MChi

187 Adsorption studies

188 Effect of pH of the solution

189 The initial pH of the dye solution is an essential controlling parameter in the adsorption process
190 because the ionic properties and structure of dye molecules may vary with varying the pH of the
191 solution. Fig. 5 shows the adsorption profiles of MG and MB onto the MChi at different pH
192 values. The outcomes showed that the solution pH had a significant effect on the adsorption of
193 dye molecules and presented that by increasing the pH of the solution from 4 – 11, the adsorption
194 capacity (removal percent) of MChi was risen significantly from 17.21 to 28.93 mg g⁻¹ (57.40 to
195 98.20 %) for MG and 26.00 to 49.07 mg g⁻¹ (52.01 to 97.90 %) for MB. These adsorption trends
196 of both the dyes can be better explained by closer inspection of pH_{pzc}, which was found to be 6.6
197 as shown in inset inset-Fig. 5. This figure displays that at pH lesser than pH_{pzc} induces a totally
198 positive charge over the surface of MChi, and causes competitive adsorption between H⁺ ions
199 and cationic dye molecules in the solution for the binding sites. Moreover, the number of
200 positively charged adsorbing sites increased with the decrease of pH, which electrostatically
201 repels the cationic dye molecules. While in the alkaline regime (pH > pH_{pzc}), the adsorption
202 capacity was increases significantly, which might be owing to the deprotonation of superficial
203 functional groups which strongly attract the cationic moiety of MG and MB molecules. It is clear
204 that the alkaline pH of the dye solution favors the adsorption of cationic dyes onto the MChi.
205 Therefore, the pH 7 for both MG and MB were chosen for further studies.



206

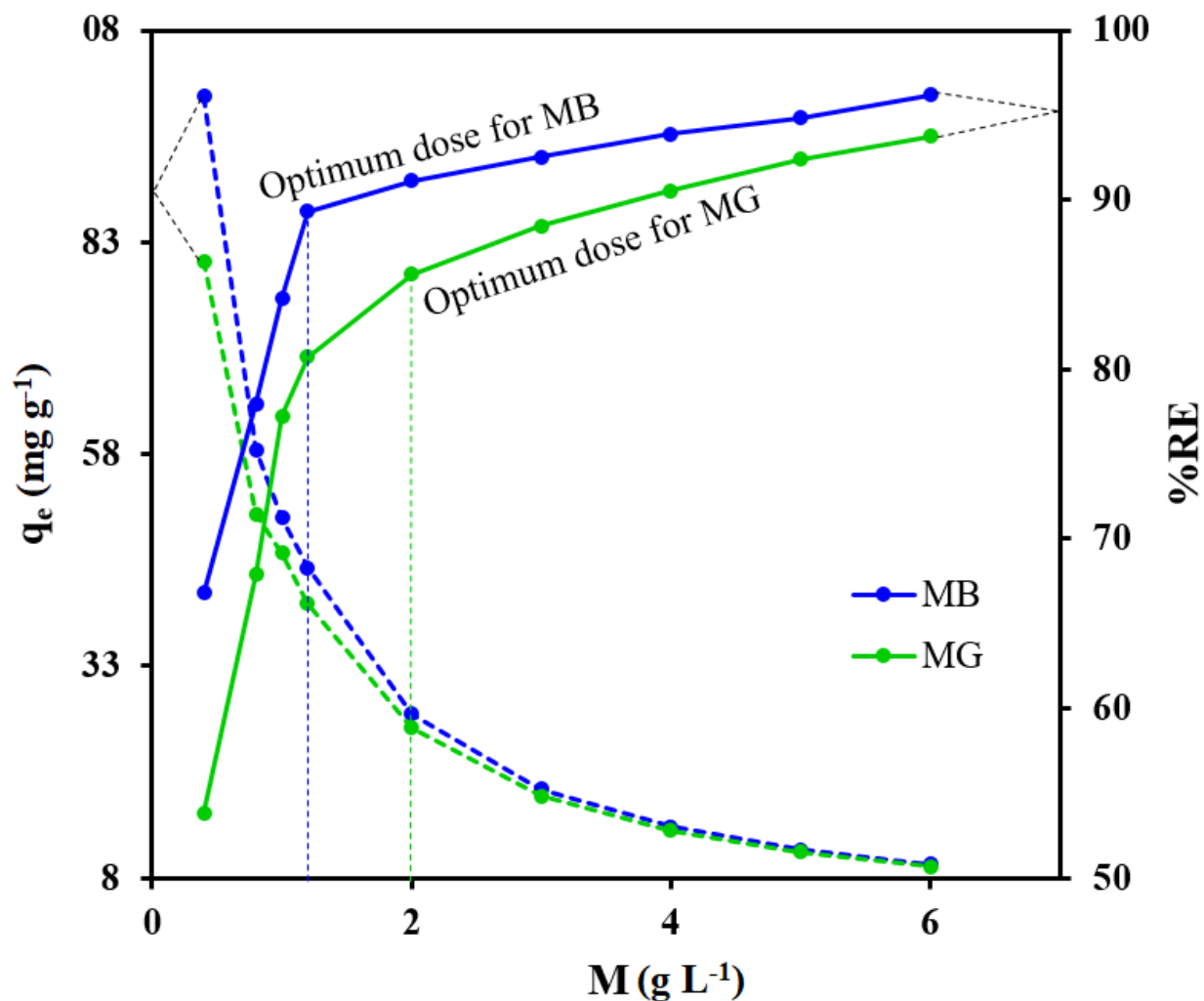
207 **Fig. 5** Effect of pH on adsorption capacity of MChs (inset–point of zero charge of MCh)

208

209 **Effect of adsorbent dose**

210 The adsorbent dose is a significant factor for determining the adsorption capacity of an
 211 adsorbent. The effect of different MChi doses of 0.4 to 6 g L⁻¹ on the adsorption of MG and MB
 212 onto the MChi was evaluated at an initial dye concentration of 50 mg g⁻¹, and the fallouts are
 213 shown in Fig. 6. This figure reveals that by increasing the quantity of MChi dose (0.4 to 6 g L⁻¹),

214 the percentage removal of both MG (53.84 to 93.73 %) and MB (66.80 to 96.20 %) was
215 increased, which may be accredited to the availability of large surface area and easy accessibility
216 of additional sorption sites. On the contrary, the adsorbate loading capacity per gram of
217 adsorbent dose declines evidently from 80.76 to 9.37 mg g⁻¹ for MG and 100.19 to 9.62 mg g⁻¹
218 for MB with the increase of adsorbent dose from 0.4 to 6.0 g L⁻¹, which was because at a higher
219 amount of MChi, the available adsorbate molecules were inadequate to cover all the active
220 adsorbing sites, thereby the adsorbing sites could not attain saturation at higher MChi dose. An
221 insufficient amount of adsorbent or overdosing would results in less adsorption or high cost,
222 thus, for economic adsorption and also by considering the influence on removal efficiency and
223 sorption capacity, compromising MChi dosage of 2.0 and 1.2 g L⁻¹ for the adsorption of MG and
224 MB, respectively were selected for further adsorption experiments.

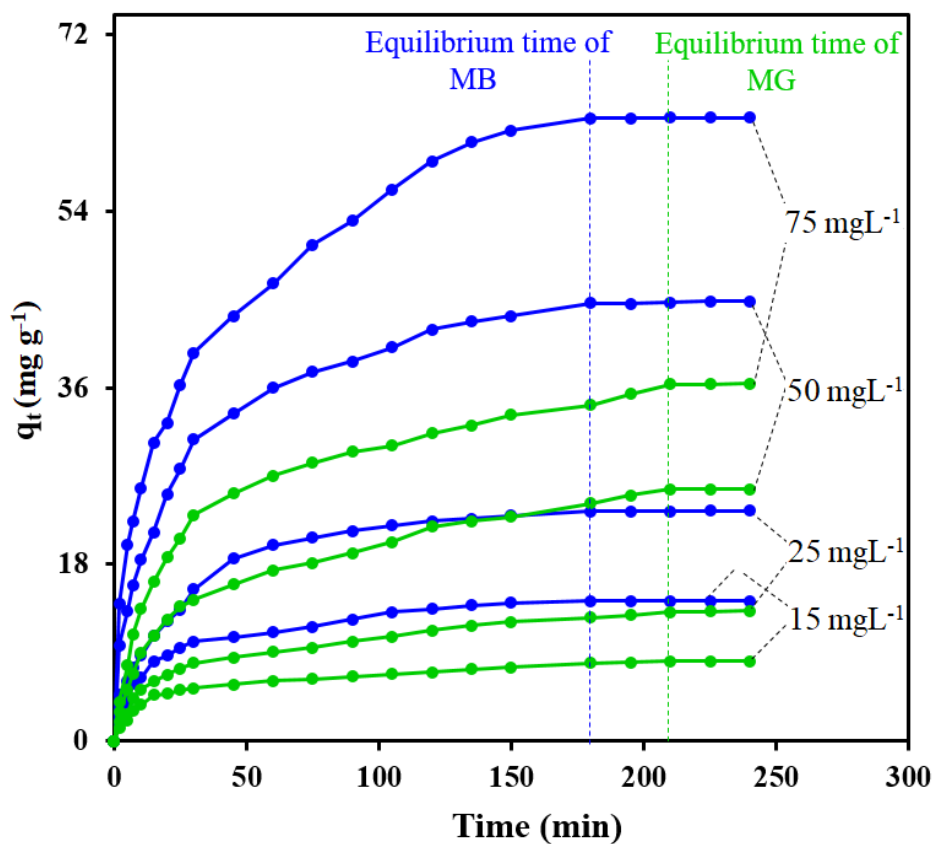


225
 226 **Fig. 6** Effect of MChs dose on adsorption capacity (q_e) and removal efficiency (% RE) of MChi
 227

228 **Effect of contact time and kinetic study**

229 The MG and MB uptake was studied with respect to time in order to observe an appropriate
 230 interaction time at which the adsorption achieves equilibrium. Fig. 7 demonstrates the influence
 231 of contact time on the adsorption of MG and MB by MChi. It is apparent from this figure that the
 232 adsorption of both MG and MB was increased initially up to 30 min at a very speedy rate due to
 233 the vacant or easy availability of the reaction sites on the external surface of MChi and with the

234 extension of adsorption time, there was a transitional phase in which the uptake process was
 235 slowed down and achieve equilibrium within 210 and 180 min for MG and MB, respectively.
 236 The slow adsorption rate at the later stage was probably owing to the lessening in the availability
 237 of the remaining active sites and also may be due to the long-range diffusion of adsorbate species
 238 into the micropores of the MChi which needs a greater time to achieve equilibrium (Du et al.
 239 2014). It is also evident from the Fig. 7 that the amount of MG and MB adsorbed onto the MChi
 240 increased with an enhancement in initial dye concentration. It is due to higher driving force for
 241 mass transfer of dye molecules from the liquid phase to the solid phases. Also, the escalation in
 242 initial concentration of dye increases the interaction between adsorbate and adsorbent and thus,
 243 increases the adsorption uptake of MG and MB dye molecules.



244

245 **Fig. 7** Effect of contact time on adsorption capacity of MChi

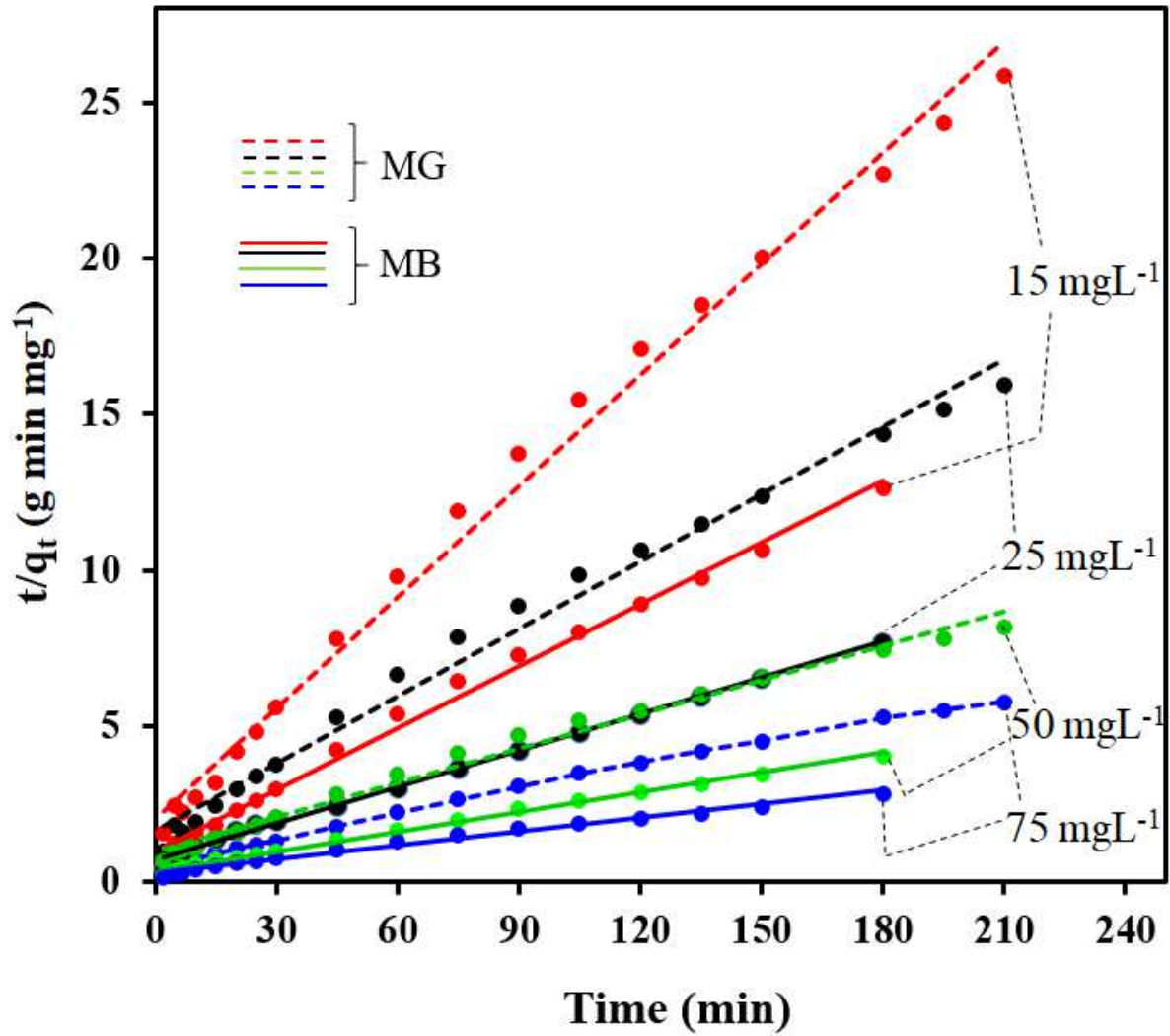
246 The time-dependent kinetic data accompanying with the adsorption of both the dyes were
247 analyzed with pseudo-Ist-order and pseudo-IInd-order models. These two models are described by
248 Eqs. 4 and 5, respectively (Mashkooor and Nasar 2020a).

$$249 \ln(q_e - q_t) = \ln q_e - K_1 t \quad (3)$$

$$250 \frac{t}{q_t} = \frac{1}{K_2 q_e^2} + \frac{t}{q_e} \quad (4)$$

251

252 where, K_1 (min^{-1}), and K_2 ($\text{g min}^{-1} \text{mg}^{-1}$) are the rate constants of the pseudo-1st-order, and
253 pseudo-2nd-order kinetic model, respectively. The kinetic parameters and correlation coefficients
254 (R^2) obtained by fitting the time-dependent experimental data for the adsorption of MG and MB
255 onto the MChi are summarized in Table 1. The R^2 values that were obtained for the pseudo-IInd-
256 order model were higher than those of the pseudo-Ist-order. Furthermore, the calculated and
257 experimental values of the adsorption capacity, q_e , were almost the same at all initial dye
258 concentration. These outcomes specify that the pseudo-IInd-order kinetic model offers a good
259 correlation for the elimination of both MG and MB onto MChi, as shown in Fig. 8. The rate-
260 limiting step might be chemisorption comprising valence forces by sharing or exchange of
261 electrons between the adsorbate and adsorbent (Bayramoglu et al. 2009). Further, as indicated
262 from Table 1, the values of pseudo-IInd-order rate constant were found to be decreased with the
263 increase of initial concentration of dye for both the system. This shows that the adsorption of
264 MG and MB onto the MChi were more favorable for low initial concentration of dye.



265

266 **Fig. 8** Pseudo-IInd-order plot for the MG and MB adsorption onto the MChi

267

268 **Table 1** Kinetic results for the MG and MB adsorption onto MChi (reaction conditions: $C_o = 50$
 269 mg L^{-1} , MChi dose = 2 g L^{-1} , pH = 7, and $T = 303 \text{ K}$ for MG and $C_o = 50 \text{ mg L}^{-1}$, MChi dose =
 270 1.2 g L^{-1} , pH = 7, and $T = 303 \text{ K}$ for MB)

271

C _o	15		25		50		75	
Dye	MG	MB	MG	MB	MG	MB	MG	MB

Pseudo-1st-order

K ₁	0.017	0.0232	0.0156	0.0272	0.0151	0.0205	0.0149	0.0214
q _{exp}	8.12	14.269	13.16	23.39	25.64	44.64	36.37	63.46
q _{cal}	5.717	10.515	10.067	16.114	20.72	31.630	26.136	50.7697
R ²	0.9356	0.9536	0.9694	0.9831	0.9564	0.9876	0.9694	0.9644

Pseudo-2nd-order

K ₂	6.878x10 ⁻³	4.3113x10 ⁻³	3.1729x10 ⁻³	2.157x10 ⁻³	1.3848x10 ⁻³	1.308x10 ⁻³	1.1897x10 ⁻³	7.7702x10 ⁻⁴
q _{exp}	8.12	14.269	13.16	23.39	25.64	44.64	36.37	63.46
q _{cal}	8.446	15.175	13.908	25.707	27.322	47.393	38.462	68.027
R ²	0.9932	0.9958	0.9899	0.9973	0.989	0.9965	0.996	0.9902

IPD

K _{id}	0.4443	0.9039	0.7803	1.6543	1.5908	2.8906	2.2107	4.1309
B	2.2097	3.6253	2.5748	4.4337	3.844	10.327	6.8808	13.137
R ²	0.9032	0.9056	0.9519	0.9248	0.9612	0.9383	0.9236	0.9764

273 Moreover, in order to assess the nature of the diffusion process for the adsorption of dyes
274 onto the MChi, the intraparticle diffusion model (IPD) was employed to evaluate the time-
275 dependent experimental data, which can be given by the following equation (Mashkooor and
276 Nasar 2019a):

$$277 \quad q_t = K_{id} \sqrt{t} + B \quad (6)$$

278

279 where, B is the intercept (mg g^{-1}), which provides the information about the thickness of the
280 boundary layer, i.e., the larger intercept, the greater is the boundary layer effect. The k_{id} is the
281 IPD rate constant ($\text{mg g}^{-1}\text{min}^{-1/2}$), which can be calculated from the slope of the q_t versus $t^{1/2}$ plot
282 (figure not shown). The IPD plot consisted of three sequential steps: the initial step of the plot
283 representing the surface adsorption and rapid external diffusion and shows the existence of the
284 boundary layer (Wang et al. 2015). The second stage corresponds to the particle diffusion, where
285 adsorbate molecules traverse within the pores of the adsorbent, and the third region is the
286 equilibrium approaching stage (Mane and Vijay Babu 2013; Tan and Hameed 2017). If the
287 regression of q_t vs $t^{1/2}$ is linear and passes through the origin, then IPD is the sole rate-controlling
288 step. The deviation of straight lines from the origin indicates that IPD is not the only rate-
289 limiting step. It can likewise be seen from the table that intercept B, increases with initial dye
290 concentration indicating the enhancement in the thickness and role of the boundary layer [36].
291 Moreover, the k_{id} values for the elimination of MB onto the MChi were higher than those for
292 MG, signifying more driving force in the former (Sewu et al. 2019).

293 **Isotherm study**

294 Adsorption isotherm was used to describe the interactive behavior and the distribution of
295 adsorbed molecules between the solution and adsorbent when the adsorption process achieves
296 equilibrium and is essential in the modeling of the adsorption system. Three different isotherms,
297 viz., Langmuir, Freundlich, and Temkin have been employed to model the experimental data.
298 The Langmuir model stated a structurally homogeneous adsorbent and monolayer coverage of
299 adsorbate over the surface of adsorbent with no interaction between the adsorbate molecules. In
300 this respect, once an adsorbate species occupies a site, no further adsorption can take place at that
301 site. This model is expressed mathematically according to the following linear equation (Zayed
302 et al. 2018; Mashkooor and Nasar 2020c).

$$303 \quad \frac{1}{q_e} = \frac{1}{q_m K_L C_e} + \frac{1}{q_m} \quad (7)$$

304 Where K_L ($L \text{ mg}^{-1}$) is the Langmuir constant, and q_m (mg g^{-1}) is the maximum monolayer
305 sorption capacity. An essential characteristic of the Langmuir isotherm can be defined by a
306 dimensionless quantity, $R_L (= \frac{1}{1+K_L C_0})$ known as separation factor, the values of which show that
307 the adsorption to be either favorable ($0 - 1$), unfavorable (> 1) or linear (1), or irreversible (0).

308 Freundlich model describes that the adsorption ensues over the heterogeneous surface by
309 multilayer adsorption and mathematically expressed in the linear form (Foo and Hameed 2010;
310 Mashkooor and Nasar 2020c):

$$311 \quad \ln q_e = \frac{1}{n} \ln C_e + \ln K_F \quad (8)$$

312 Where, K_f (mg g^{-1}) shows adsorption capacity, and n is an empirical factor associated to the
313 intensity of adsorption, which varies with the heterogeneity of the adsorbing material. The larger
314 value of the n , favors the adsorption.

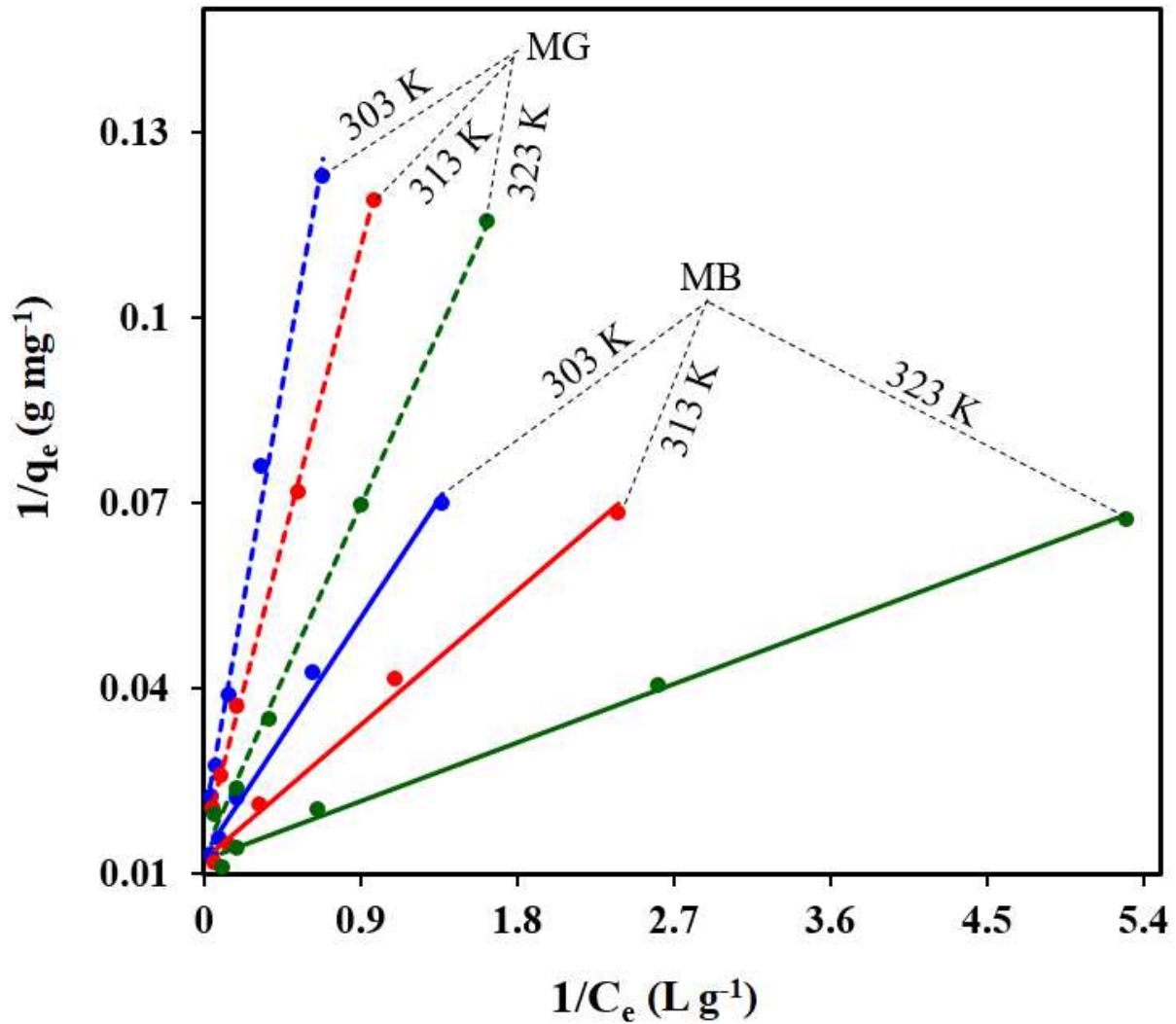
315 The Temkin model takes into account that the adsorbate-adsorbent interaction causes the
316 linear reduction in the heat of adsorption rather than in logarithmic form. This model can be
317 represented by linear form as (Foo and Hameed 2010):

$$318 \quad q_e = B \ln C_e + B \ln K_T \quad (10)$$

319 where, K_T ($L g^{-1}$) is the equilibrium binding constant related to the maximum binding energy,
320 and B ($=RT/b$), b ($J mol^{-1}$) is the Temkin isotherm constants. R ($= 8.314 J K^{-1} mol^{-1}$) is the
321 universal gas constant and T (K) is the absolute temperature.

322 The isotherm parameters, as obtained by fitting the equilibrium parameters for the
323 adsorption of MG and MB onto the MChi, are given in Table 2. In the light of higher values of
324 R^2 , the Langmuir model is proposed to be best fit for both the systems (MG/MChi and
325 MB/MChi) at all temperatures implying monolayer coverage of MG and MB molecules onto the
326 surface of MChi as illustrated in Fig. 9. Moreover, the values of q_m increase with the increase of
327 temperature, signifying an endothermic nature of the existing adsorption process. Besides, the
328 values of R_L at an initial MG and MB concentration of 15, 25, 50, 75, and 100 $mg L^{-1}$ were
329 found to be 0.3705, 0.2609, 0.1500, 0.1053, and 0.0811 for MG and 0.1781, 0.1151, 0.0611,
330 0.0416 and 0.0315 for MB, respectively at 303 K. These values are in the range of 0 to 1, which
331 points out the favorability of the adsorption process for both the system.

332 Some of the literature work on the elimination of MG (Bekçi et al. 2008; Debrassi et al.
333 2012; Li et al. 2015; Naseeruteen et al. 2018; Arumugam et al. 2019; Hasan et al. 2020) and MB
334 (Yan et al. 2013; Zeng et al. 2015; Cho et al. 2015; Marrakchi et al. 2016; Rahmi et al. 2019;
335 Mokhtar et al. 2020) onto the chitosan-based composites are listed in Table 3. This table
336 demonstrates the satisfactory performance of the present adsorbent, MChi.



337

338 **Fig. 9** Langmuir model for the MG and MB adsorption onto the MChi

339

340 **Table 2** Isotherm parameters for the MG and MB adsorption onto MChi at different temperature

341 (reaction condition: MChs dose = 2 g L⁻¹, t = 210 min, pH = 7 for MG and MChi dose = 1.2 g L⁻¹,

342 t = 180 min, pH = 7 for MB)

Temperature (K)	303		313		323	
Adsorbate	MG	MB	MG	MB	MG	MB
Langmuir						

q_m	55.8659	76.3359	62.893	81.3008	74.0741	82.645
K_L	0.113291	0.30751	0.150711	0.508265	0.2160	1.141511
R^2	0.9924	0.9921	0.9995	0.9931	0.9984	0.994
Freundlich						
N	1.64258	2.0333	1.6761	2.05719	1.80473	2.2727
K_F	6.79237	17.9376	9.0784	24.320	13.50419	34.8168
R^2	0.9829	0.9854	0.9859	0.9804	0.9279	0.9794
Temkin						
B	13.067	18.371	13.703	19.411	13.585	18.430
K_T	1.07636	2.53436	1.58636	4.292657	3.008924	10.34738
R^2	0.9863	0.9894	0.9897	0.9895	0.9797	0.9837

343

344 **Table 3** Comparison of Langmuir factors for the adsorption of MG and MB on the Chi based
345 adsorbents

Adsorbent	q_m (mg g ⁻¹)	K_L (L mg ⁻¹)	R^2	References
Malachite green				
Coir pith activated carbon/chitosan/sodium dodecyl sulphate	4.8	0.1	0.999	(Arumugam et al. 2019)
Polyacrylamide-g-chitosan γ -Fe ₂ O ₃	62.89	0.25	0.990	(Hasan et al. 2020)
Chitosan bead	93.55	0.41	0.982	(Bekçi et al. 2008)

Chitosan ionic liquid beads	8.07	-12.399	0.998	(Naseeruteen et al. 2018)
Polyurethane/chitosan composite foam	16.67	0.78*	0.9756	(Li et al. 2015)
N-benzyl-O-carboxymethylchitosan magnetic nanoparticles	99.82	0.474	0.927	(Debrassi et al. 2012)
MChi	55.87	0.11329	0.9924	Present work
Methylene blue				
H ₂ SO ₄ crosslinked magnetic chitosan	20.408	0.018	0.998	(Rahmi et al. 2019)
Chitosan/clay/Fe ₃ O ₄	45.1	0.1897	0.907	(Cho et al. 2015)
Crosslinked chitosan/sepiolite	40.986	0.680	0.915	(Marrakchi et al. 2016)
Magadiite-chitosan composite beads	40.01	0.014	0.995	(Mokhtar et al. 2020)
Chitosan/organic rectorite	24.69	0.242	0.999	(Zeng et al. 2015)
Chitosan magnetic composite microspheres	33.60	4.26x10 ²	0.995	(Yan et al. 2013)
MChi	76.34	0.3075	0.9921	Present work

346 *ml μg⁻¹

347

348 **Thermodynamic study**

349 To understand the influence of temperature on the adsorption of MG and MB onto the MChi, the
350 adsorption experiments were accompanied at 303, 313, 323 and 333 K. The thermodynamic
351 factors such as Gibb's free energy change (ΔG), enthalpy change (ΔH), and entropy change (ΔS)
352 were measured by employing the following Van't Hoff equation (Mashkooor and Nasar 2019b;
353 Ahmed et al. 2020).

$$354 \quad \Delta G = -RT \ln K_c \quad (19)$$

$$355 \quad \ln K_c = \frac{-\Delta G}{RT} = \frac{-\Delta H}{RT} + \frac{\Delta S}{R} \quad (20)$$

356 where, K_c represents equilibrium constant. The parameters ΔH and ΔS were calculated
357 respectively from the slope and intercept of van't Hoff plot of $\ln K_c$ versus $1/T$ (figure not given).
358 All the values of the thermodynamic parameters are listed in Table 4. The negative values of ΔG
359 for both MG and MB over the entire temperature range (303 to 333 K) demonstrated the
360 underlying spontaneity and confirmed the feasibility of the adsorption process. In other words, a
361 large negative value of ΔG infers a greater driving force of adsorption, ensuing in improved
362 adsorption capacity. From Table 4, the ΔG value was resulted to be more negative at higher
363 temperatures, suggesting that the process for the elimination of both MG and MB was more
364 spontaneous at higher temperatures. In fact, ΔG for chemisorption is greater than that for
365 physisorption. The former is between -80 and -400 kJ mol^{-1} , and the latter is between -20 to 0 kJ
366 mol^{-1} (Kuo et al. 2008; Tehrani-Bagha et al. 2011). In this research, the negative values of ΔG
367 for MG range from 7.24 to 14.08 kJ mol^{-1} and 6.44 to 11.29 kJ mol^{-1} for MB, representing that
368 physisorption is dominant in both the system. Besides, the ΔH value is positive in both cases,
369 suggesting an endothermic nature of the process. As $\Delta H > 0$, i.e., higher temperature will favor
370 the elimination of MG and MB by MChi. Moreover, the higher value of ΔH for MB than that of

371 MG signifying that the interaction between MB and MChi was stronger and led to more
 372 significant adsorption (Bayramoglu et al. 2009). The positive value of ΔS discloses the increase
 373 in the degree of freedom at the solid-liquid interface during the fixation of adsorbate on the
 374 adsorbing site of the MChi.

375

376 **Table 4** Thermodynamic parameters for the MG and MB adsorption onto MChi (reaction
 377 condition: $C_o = 50 \text{ mg L}^{-1}$, MChi dose = 2 g L^{-1} , pH = 7, t = 210 min for MG and $C_o = 50 \text{ mg L}^{-1}$,
 378 MChi dose = 1.2 g L^{-1} , pH = 7, t = 180 min for MB)

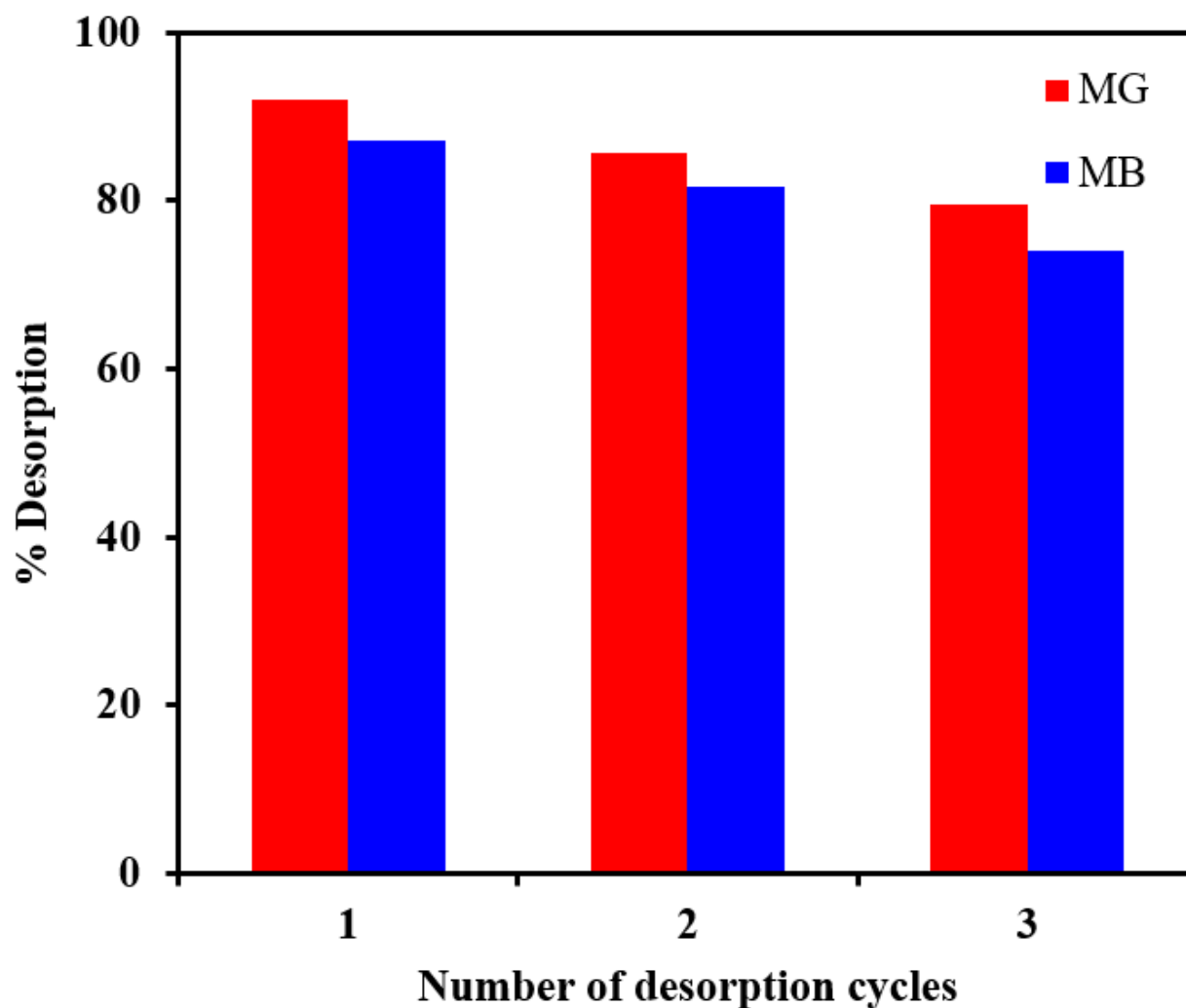
	MB				MG			
T (K)	303	313	323	333	303	313	323	333
$-\Delta G \text{ (kJ mol}^{-1}\text{)}$	7.236	8.905	11.185	14.078	6.438	7.521	9.637	11.291
$\Delta H \text{ (kJ mol}^{-1}\text{)}$	61.683				44.065			
$\Delta S \text{ (J K}^{-1} \text{ mol}^{-1}\text{)}$	226.523				165.997			

379

380 **Desorption and regeneration study**

381 The economic viability of using adsorbent to eliminate pollutants from aqueous media depends
 382 on its regeneration ability during repeated ad-/de-sorption cycles. In this research, various
 383 desorbing agents ($\text{C}_2\text{H}_5\text{OH}$ and 0.1 M HCl) were used in the batch system in order to determine a
 384 suitable eluent for the desorption of cationic dyes (MG and MB) from the MChi. The findings
 385 show that the maximum desorption for MG and MB was obtained with ethanol, and nearly 92.09
 386 and 87.06 % respectively, desorption was achieved under this condition as revealed in Fig. 10.

387 The MChi was again subjected to adsorption experiments at the optimum conditions, and the ad-
388 /de-sorption cycles were repeated three times. The results (Fig. 10) showed that the desorption
389 percentage of MG and MB from the MChi was about 79.56 and 74.06 % up to three cycles, with
390 the adsorption percentage of 67.57 and 73.31 %, respectively.



391

392 **Fig. 10** Reusability of MChi after adsorption of MG and MB

393

394

395

396 **Conclusion**

397 The present research emphasizes on the adsorption potential of magnetized chitosan (MChi)
398 towards the removal of cationic MG and MB dyes from aqueous media. The time-dependent
399 experimental data illustrated that 85.45 and 89.29 % of the MG and MB could be eliminated
400 within 210 and 180 min, respectively, which confirms its prospect for practical application. It
401 was perceived that MChi showed a greater adsorption efficiency for MB than MG. The higher
402 values of the correlation coefficient revealed that the adsorption process of dyes onto the MChi
403 followed Langmuir isotherms and pseudo-IInd-order kinetic models. The maximum monolayer
404 adsorption capacity for MG and MB dyes was obtained to be 55.87 and 76.34 mg g⁻¹,
405 respectively at 303 K. Thermodynamic analysis revealed that adsorption of both the dyes was
406 spontaneous and endothermic in nature. The desorption experiments unveiled that the MChi after
407 adsorption of MG and MB could be regenerated easily by ethanol. Overall, it can be concluded
408 that MChi fulfills the criteria of a probable adsorbent for MG and MB adsorption from
409 wastewater.

410

411 **Acknowledgments**

412 The authors thank the Chairperson of the Department of Applied Chemistry, Faculty of
413 Engineering and Technology, AMU, for extending laboratory facilities.

414

415 **Data availability** Not applicable

416 **Ethics approval and consent to participate** Not applicable

417 **Conflict of interest**

418 The authors declare that they have no conflict of interests.

419 **Funding information**

420 Not applicable

421 **Author Contributions** Fouzia Mashkoo: Methodology, investigation, interpretation of
422 experimental data, formal analysis, writing – original draft,

423 Abu Nasar: Conceptualisation, supervision, interpretation of experimental data, writing -
424 review and editing, manuscript administration

425

426 **Competing Interests**

427 The authors declare no competing interests.

428

429

430

431

432

433

434

435

436

437

438

439

440

441

442
443
444
445
446
447
448
449
450
451
452
453
454
455
456
457
458
459
460
461
462
463
464
465
466
467
468
469
470
471
472
473
474
475
476

References

- Agarwal A, Verma AK, Yoshida M, et al (2020) A novel catalytic kinetic method for the determination of mercury (II) in water samples. *RSC Adv* 10:25100–25106. doi: 10.1039/D0RA03487H
- Ahmed M, Mashkoo F, Nasar A (2020) Development, characterization, and utilization of magnetized orange peel waste as a novel adsorbent for the confiscation of crystal violet dye from aqueous solution. *Groundw Sustain Dev* 10:100322. doi: 10.1016/j.gsd.2019.100322
- Arumugam TK, Krishnamoorthy P, Rajagopalan NR, et al (2019) Removal of malachite green from aqueous solutions using a modified chitosan composite. *Int J Biol Macromol* 128:655–664. doi: 10.1016/j.ijbiomac.2019.01.185
- Bagheri H, Roostaie A, Baktash MY (2014) A chitosan-polypyrrole magnetic nanocomposite as μ -sorbent for isolation of naproxen. *Anal Chim Acta* 816:1–7. doi: 10.1016/j.aca.2014.01.028
- Bayramoglu G, Altintas B, Arica MY (2009) Adsorption kinetics and thermodynamic parameters of cationic dyes from aqueous solutions by using a new strong cation-exchange resin. *Chem Eng J* 152:339–346. doi: 10.1016/j.cej.2009.04.051
- Bekçi Z, Özveri C, Seki Y, Yurdakoç K (2008) Sorption of malachite green on chitosan bead. *J Hazard Mater* 154:254–261. doi: 10.1016/j.jhazmat.2007.10.021
- Cabuk M, Alan Y, Yavuz M, Unal HI (2014) Synthesis, characterization and antimicrobial activity of biodegradable conducting polypyrrole-graft-chitosan copolymer. *Appl Surf Sci* 318:168–175. doi: 10.1016/j.apsusc.2014.02.180
- Cao C, Xiao L, Chen C, et al (2014) In situ preparation of magnetic Fe₃O₄/chitosan nanoparticles via a novel reduction–precipitation method and their application in adsorption of reactive azo dye. *Powder Technol* 260:90–97. doi: 10.1016/j.powtec.2014.03.025
- Chen B, Zhao H, Chen S, et al (2019) A magnetically recyclable chitosan composite adsorbent functionalized with EDTA for simultaneous capture of anionic dye and heavy metals in complex wastewater. *Chem Eng J* 356:69–80. doi: 10.1016/j.cej.2018.08.222
- Cho D-W, Jeon B-H, Chon C-M, et al (2015) Magnetic chitosan composite for adsorption of cationic and anionic dyes in aqueous solution. *J Ind Eng Chem* 28:60–66. doi: 10.1016/j.jiec.2015.01.023

- 477 Debrassi A, Corrêa AF, Baccarin T, et al (2012) Removal of cationic dyes from aqueous
478 solutions using N-benzyl-O-carboxymethylchitosan magnetic nanoparticles. *Chem Eng J*
479 183:284–293. doi: 10.1016/j.cej.2011.12.078
- 480 Du Q, Sun J, Li Y, et al (2014) Highly enhanced adsorption of congo red onto graphene
481 oxide/chitosan fibers by wet-chemical etching off silica nanoparticles. *Chem Eng J* 245:99–
482 106. doi: 10.1016/j.cej.2014.02.006
- 483 Fan L, Luo C, Li X, et al (2012) Fabrication of novel magnetic chitosan grafted with graphene
484 oxide to enhance adsorption properties for methyl blue. *J Hazard Mater* 215–216:272–279.
485 doi: 10.1016/j.jhazmat.2012.02.068
- 486 Foo KY, Hameed BH (2010) Insights into the modeling of adsorption isotherm systems. *Chem*
487 *Eng J* 156:2–10. doi: 10.1016/j.cej.2009.09.013
- 488 Franco EG, Kastner A, Kuritzky M, Lukacs R (2019) Regional risks for doing business 2019.
489 *World Econ Forum* 1–40.
- 490 Hasan I, Bhatia D, Walia S, Singh P (2020) Removal of malachite green by polyacrylamide-g-
491 chitosan γ -Fe₂O₃ nanocomposite-an application of central composite design. *Groundw*
492 *Sustain Dev* 11:100378. doi: 10.1016/j.gsd.2020.100378
- 493 Hokkanen S, Bhatnagar A, Sillanpää M (2016) A review on modification methods to cellulose-
494 based adsorbents to improve adsorption capacity. *Water Res* 91:156–173. doi:
495 10.1016/j.watres.2016.01.008
- 496 Ippolito A, Fait G (2019) Pesticides in surface waters: from edge-of-field to global modelling.
497 *Curr Opin Environ Sustain* 36:78–84. doi: 10.1016/j.cosust.2018.10.023
- 498 Jafari S, Zhao F, Zhao D, et al (2015) A comparative study for the removal of methylene blue
499 dye by N and S modified TiO₂ adsorbents. *J Mol Liq* 207:90–98. doi:
500 10.1016/j.molliq.2015.03.026
- 501 Jain SN, Shaikh Z, Mane VS, et al (2019) Nonlinear regression approach for acid dye
502 remediation using activated adsorbent: Kinetic, isotherm, thermodynamic and reusability
503 studies. *Microchem J* 148:605–615. doi: 10.1016/j.microc.2019.05.024
- 504 Jain SN, Tamboli SR, Sutar DS, et al (2020) Batch and continuous studies for adsorption of
505 anionic dye onto waste tea residue: Kinetic, equilibrium, breakthrough and reusability
506 studies. *J Clean Prod* 252:119778. doi: 10.1016/j.jclepro.2019.119778
- 507 Kang S, Qin L, Zhao Y, et al (2020) Enhanced removal of methyl orange on exfoliated
508 montmorillonite/chitosan gel in presence of methylene blue. *Chemosphere* 238:124693. doi:
509 10.1016/j.chemosphere.2019.124693
- 510 Kant R (2012) Textile dyeing industry an environmental hazard. *Nat Sci* 4:22–26. doi:
511 10.4236/ns.2012.41004
- 512 Kazeminezhad I, Mosivand S (2014) Phase Transition of Electrooxidized Fe₃O₄ to γ and α -Fe₂O₃
513 Nanoparticles Using Sintering Treatment. *Acta Phys Pol A* 125:1210–1214. doi:

514 10.12693/APhysPolA.125.1210

515 Kuo C-Y, Wu C-H, Wu J-Y (2008) Adsorption of direct dyes from aqueous solutions by carbon
516 nanotubes: Determination of equilibrium, kinetics and thermodynamics parameters. *J*
517 *Colloid Interface Sci* 327:308–315. doi: 10.1016/j.jcis.2008.08.038

518 Lehman JH, Terrones M, Mansfield E, et al (2011) Evaluating the characteristics of multiwall
519 carbon nanotubes. *Carbon N Y* 49:2581–2602. doi: 10.1016/j.carbon.2011.03.028

520 Li X, Li J, Sun X, et al (2015) Preparation and malachite green adsorption behavior of
521 polyurethane/chitosan composite foam. *J Cell Plast* 51:373–386. doi:
522 10.1177/0021955X14542538

523 Lou T, Yan X, Wang X (2019) Chitosan coated polyacrylonitrile nanofibrous mat for dye
524 adsorption. *Int J Biol Macromol* 135:919–925. doi: 10.1016/j.ijbiomac.2019.06.008

525 Mane VS, Vijay Babu PV (2013) Kinetic and equilibrium studies on the removal of Congo red
526 from aqueous solution using Eucalyptus wood (*Eucalyptus globulus*) saw dust. *J Taiwan*
527 *Inst Chem Eng* 44:81–88. doi: 10.1016/j.jtice.2012.09.013

528 Marrakchi F, Khanday WA, Asif M, Hameed BH (2016) Cross-linked chitosan/sepiolite
529 composite for the adsorption of methylene blue and reactive orange 16. *Int J Biol Macromol*
530 93:1231–1239. doi: 10.1016/j.ijbiomac.2016.09.069

531 Mashkoo F, Nasar A (2020a) Magsorbents: Potential candidates in wastewater treatment
532 technology – A review on the removal of methylene blue dye. *J. Magn. Magn. Mater.*
533 500:166408.

534 Mashkoo F, Nasar A (2020b) Facile synthesis of polypyrrole decorated chitosan-based
535 magsorbent: Characterizations, performance, and applications in removing cationic and
536 anionic dyes from aqueous medium. *Int J Biol Macromol* 161:88–100. doi:
537 10.1016/j.ijbiomac.2020.06.015

538 Mashkoo F, Nasar A (2019a) Preparation, characterization and adsorption studies of the
539 chemically modified *Luffa aegyptica* peel as a potential adsorbent for the removal of
540 malachite green from aqueous solution. *J Mol Liq* 274:315–327. doi:
541 10.1016/j.molliq.2018.10.119

542 Mashkoo F, Nasar A (2020c) Magnetized *Tectona grandis* sawdust as a novel adsorbent:
543 preparation, characterization, and utilization for the removal of methylene blue from
544 aqueous solution. *Cellulose*. doi: 10.1007/s10570-019-02918-8

545 Mashkoo F, Nasar A (2019b) Polyaniline/*Tectona grandis* sawdust: A novel composite for
546 efficient decontamination of synthetically polluted water containing crystal violet dye.
547 *Groundw Sustain Dev* 8:390–401. doi: 10.1016/j.gsd.2018.12.008

548 Mashkoo F, Nasar A, Inamuddin (2020) Carbon nanotube-based adsorbents for the removal of
549 dyes from waters: A review. *Environ Chem Lett*. doi: 10.1007/s10311-020-00970-6

550 Mashkoo F, Nasar A, Inamuddin, Asiri AM (2018) Exploring the reusability of synthetically

551 contaminated wastewater containing crystal violet dye using *Tectona grandis* sawdust as a
552 very low-cost adsorbent. *Sci Rep* 8:8314. doi: 10.1038/s41598-018-26655-3

553 Mokhtar A, Abdelkrim S, Djelad A, et al (2020) Adsorption behavior of cationic and anionic
554 dyes on magadiite-chitosan composite beads. *Carbohydr Polym* 229:115399. doi:
555 10.1016/j.carbpol.2019.115399

556 Nasar A, Mashkoo F (2019) Application of polyaniline-based adsorbents for dye removal from
557 water and wastewater—a review. *Environ Sci Pollut Res* 26:5333–5356. doi:
558 10.1007/s11356-018-3990-y

559 Naseeruteen F, Hamid NSA, Suah FBM, et al (2018) Adsorption of malachite green from
560 aqueous solution by using novel chitosan ionic liquid beads. *Int J Biol Macromol* 107:1270–
561 1277. doi: 10.1016/j.ijbiomac.2017.09.111

562 Novais RM, Ascensão G, Tobaldi DM, et al (2018) Biomass fly ash geopolymer monoliths for
563 effective methylene blue removal from wastewaters. *J Clean Prod* 171:783–794. doi:
564 10.1016/j.jclepro.2017.10.078

565 Prasad AR, Joseph A (2017) Synthesis, characterization and investigation of methyl orange dye
566 removal from aqueous solutions using waterborne poly vinyl pyrrolidone (PVP) stabilized
567 poly aniline (PANI) core–shell nanoparticles. *RSC Adv* 7:20960–20968. doi:
568 10.1039/C7RA01790A

569 Qamruzzaman, Nasar A (2015) Degradation of acephate by colloidal manganese dioxide in the
570 absence and presence of surfactants. *Desalin Water Treat* 55:2155–2164. doi:
571 10.1080/19443994.2014.937752

572 Qamruzzaman, Nasar A (2019) Degradative treatment of bispyribac sodium herbicide from
573 synthetically contaminated water by colloidal MnO₂ dioxide in the absence and presence of
574 surfactants. *Environ Technol* 40:451–457. doi: 10.1080/09593330.2017.1396500

575 Qi L, Tang X, Wang Z, Peng X (2017) Pore characterization of different types of coal from coal
576 and gas outburst disaster sites using low temperature nitrogen adsorption approach. *Int J*
577 *Min Sci Technol* 27:371–377. doi: 10.1016/j.ijmst.2017.01.005

578 Quesada HB, Baptista ATA, Cusioli LF, et al (2019) Surface water pollution by pharmaceuticals
579 and an alternative of removal by low-cost adsorbents: A review. *Chemosphere* 222:766–
580 780. doi: 10.1016/j.chemosphere.2019.02.009

581 Rahmi, Ishmaturrehmi, Mustafa I (2019) Methylene blue removal from water using H₂SO₄
582 crosslinked magnetic chitosan nanocomposite beads. *Microchem J* 144:397–402. doi:
583 10.1016/j.microc.2018.09.032

584 Sabar S, Aziz HA, Yusof NH, et al (2020) Preparation of sulfonated chitosan for enhanced
585 adsorption of methylene blue from aqueous solution. *React Funct Polym* 104584. doi:
586 10.1016/j.reactfunctpolym.2020.104584

587 Saravanakumar R, Muthukumaran K, Selvaraju N (2019) Enhanced Pb (II) ions removal by
588 using magnetic NiO/Biochar composite. *Mater Res Express* 6:105504. doi: 10.1088/2053-

589 1591/ab2141

- 590 Sewu DD, Jung H, Kim SS, et al (2019) Decolorization of cationic and anionic dye-laden
591 wastewater by steam-activated biochar produced at an industrial-scale from spent
592 mushroom substrate. *Bioresour Technol* 277:77–86. doi: 10.1016/j.biortech.2019.01.034
- 593 Shakoor S, Nasar A (2016) Removal of methylene blue dye from artificially contaminated water
594 using citrus limetta peel waste as a very low cost adsorbent. *J Taiwan Inst Chem Eng*
595 66:154–163. doi: 10.1016/j.jtice.2016.06.009
- 596 Shakoor S, Nasar A (2017) Adsorptive treatment of hazardous methylene blue dye from
597 artificially contaminated water using cucumis sativus peel waste as a low-cost adsorbent.
598 *Groundw Sustain Dev* 5:152–159. doi: 10.1016/j.gsd.2017.06.005
- 599 Tan KL, Hameed BH (2017) Insight into the adsorption kinetics models for the removal of
600 contaminants from aqueous solutions. *J Taiwan Inst Chem Eng* 74:25–48. doi:
601 10.1016/j.jtice.2017.01.024
- 602 Tehrani-Bagha AR, Nikkar H, Mahmoodi NM, et al (2011) The sorption of cationic dyes onto
603 kaolin: Kinetic, isotherm and thermodynamic studies. *Desalination* 266:274–280. doi:
604 10.1016/j.desal.2010.08.036
- 605 Tomar V, Prasad S, Kumar D (2014) Adsorptive removal of fluoride from aqueous media using
606 *Citrus limonum* (lemon) leaf. *Microchem J* 112:97–103. doi: 10.1016/j.microc.2013.09.010
- 607 Vakili M, Deng S, Cagnetta G, et al (2019) Regeneration of chitosan-based adsorbents used in
608 heavy metal adsorption: A review. *Sep Purif Technol* 224:373–387. doi:
609 10.1016/j.seppur.2019.05.040
- 610 Wang P, Ma Q, Hu D, Wang L (2015) Removal of Reactive Blue 21 onto magnetic chitosan
611 microparticles functionalized with polyamidoamine dendrimers. *React Funct Polym* 91–
612 92:43–50. doi: 10.1016/j.reactfunctpolym.2015.04.007
- 613 Yan H, Li H, Yang H, et al (2013) Removal of various cationic dyes from aqueous solutions
614 using a kind of fully biodegradable magnetic composite microsphere. *Chem Eng J* 223:402–
615 411. doi: 10.1016/j.cej.2013.02.113
- 616 Zayed AM, Abdel Wahed MSM, Mohamed EA, Sillanpää M (2018) Insights on the role of
617 organic matters of some Egyptian clays in methyl orange adsorption: Isotherm and kinetic
618 studies. *Appl Clay Sci* 166:49–60. doi: 10.1016/j.clay.2018.09.013
- 619 Zeng L, Xie M, Zhang Q, et al (2015) Chitosan/organic rectorite composite for the magnetic
620 uptake of methylene blue and methyl orange. *Carbohydr Polym* 123:89–98. doi:
621 10.1016/j.carbpol.2015.01.021
- 622 Zhao F, Repo E, Yin D, et al (2015) EDTA-cross-linked β -cyclodextrin: An environmentally
623 friendly bifunctional adsorbent for simultaneous adsorption of metals and cationic dyes.
624 *Environ Sci Technol* 49:10570–10580. doi: 10.1021/acs.est.5b02227
- 625 Zhao F, Repo E, Yin D, Sillanpää MET (2013) Adsorption of Cd(II) and Pb(II) by a novel

626 EGTA-modified chitosan material: Kinetics and isotherms. *J Colloid Interface Sci* 409:174–
627 182. doi: 10.1016/j.jcis.2013.07.062

628 Zhu Y, Xue J, Xu T, et al (2017) Enhanced photocatalytic activity of magnetic core–shell
629 $\text{Fe}_3\text{O}_4@\text{Bi}_2\text{O}_3$ -RGO heterojunctions for quinolone antibiotics degradation under visible
630 light. *J Mater Sci Mater Electron* 28:8519–8528. doi: 10.1007/s10854-017-6574-6

631

632

633

634

635

636

637

638

639

640

641

642

643

644

Figures

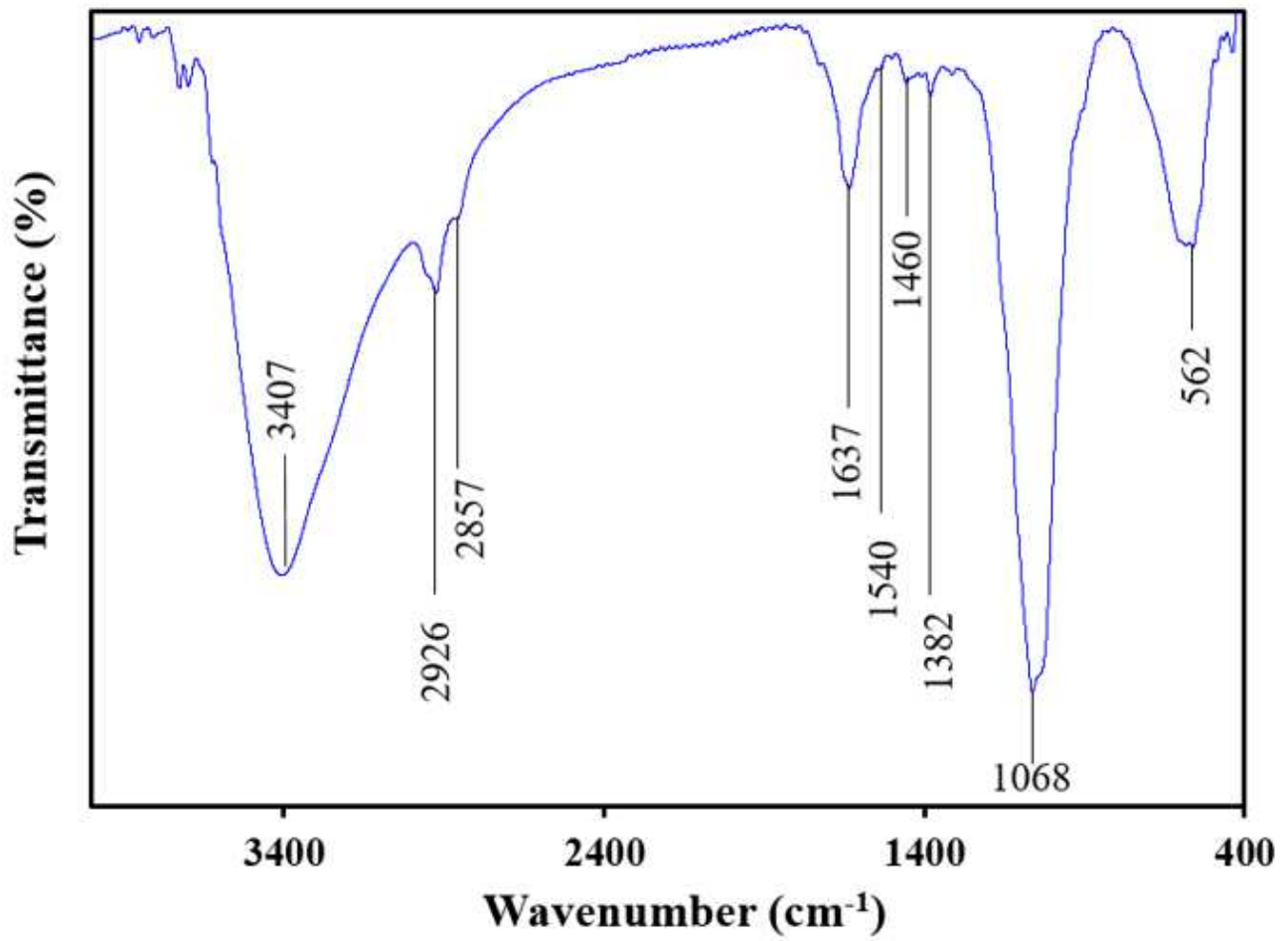


Figure 1

(a) FTIR of MChi

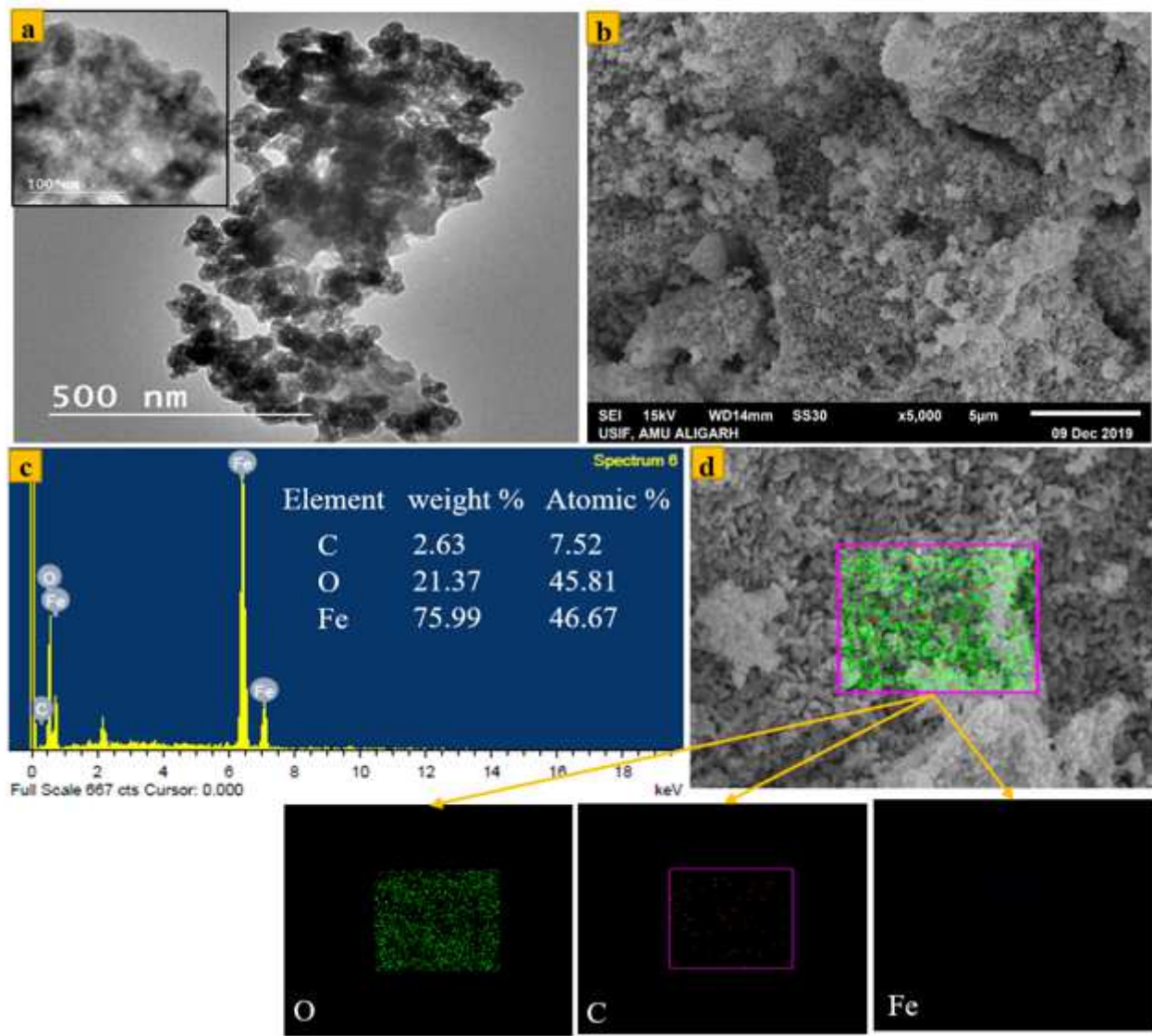
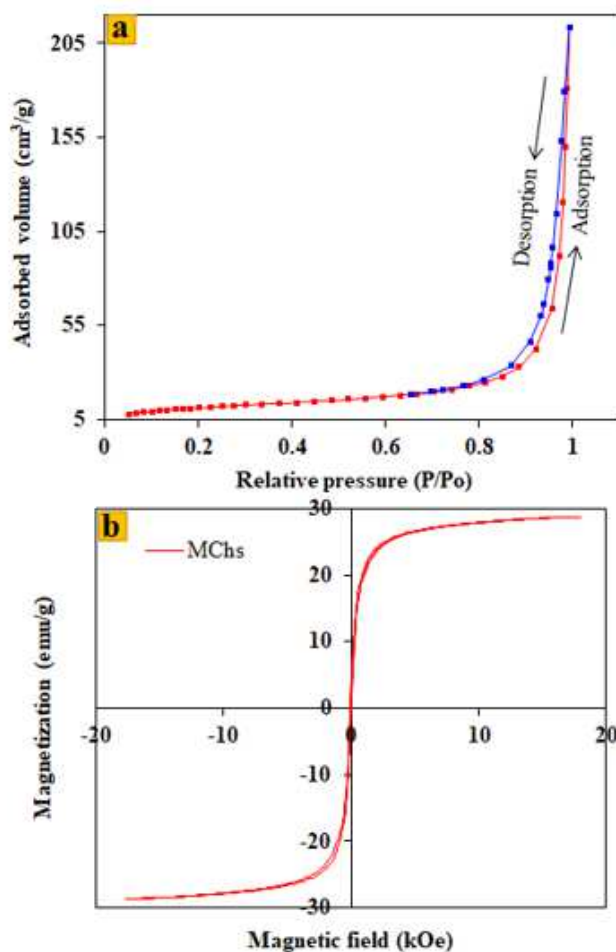


Figure 2

(a) TEM images (b) SEM image (c) EDAX image (d) Elemental mapping of MChi



(a') Summary of the BET analysis of MChi

Parameters	Values
Single-point surface area at $P/P_0=0.3001$	38.4813 m ² /g
Single-point adsorption total pore volume of the pores (pores less than 2988.714 Å diameter at $P/P_0=0.993559$)	0.33003 cm ³ /g
BET surface area	39.9930 m ² /g
Adsorption average pore width (4V/A by BET)	33.00897 nm
t-plot external surface area	39.1537 m ² /g
t-plot micropore area	0.8393 m ² /g
t-plot micropore volume	0.000187 cm ³ /g
BJH adsorption cumulative surface area of pores between 17-3000 Å diameter	33.553 m ² /g
BJH adsorption average pore width (4V/A by BET)	38.9751 nm
BJH desorption cumulative surface area of pores between 17-3000 Å diameter	36.7427 m ² /g
BJH desorption average pore width (4V/A by BET)	35.8733 nm

(b') Magnetic properties of MChi

Parameters	Values
Coercivity (Hc)	54.507 Oe
Magnetization (Ms)	28.645 emu/g
Retentivity (M)	2.9258 emu/g

Figure 3

(a) N₂ ad-/de-sorption isotherm, (a') Summary of the BET analyses (b) Magnetization curve (b') Magnetic properties of MChi

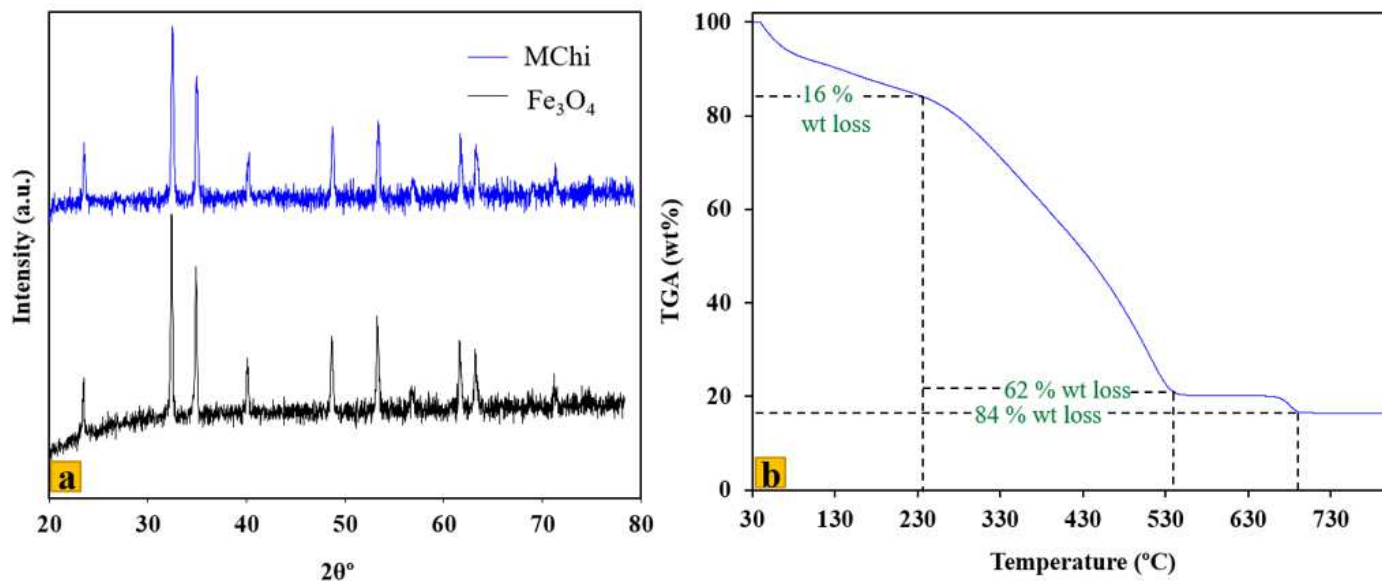


Figure 4

XRD patterns of Fe₃O₄, and MChi (b) TGA plot of MChi

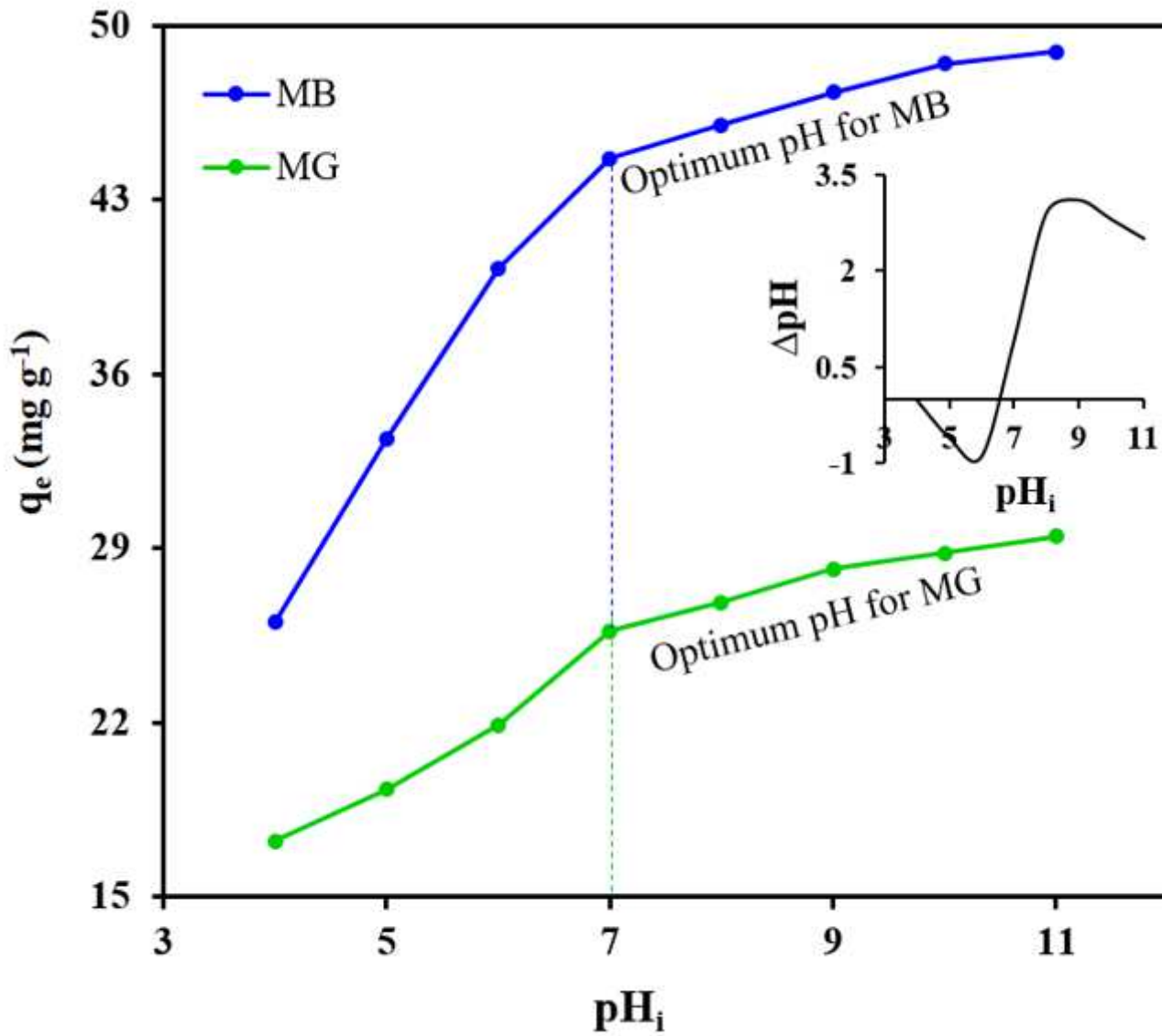


Figure 5

Effect of pH on adsorption capacity of MChs (inset–point of zero charge of MChI)

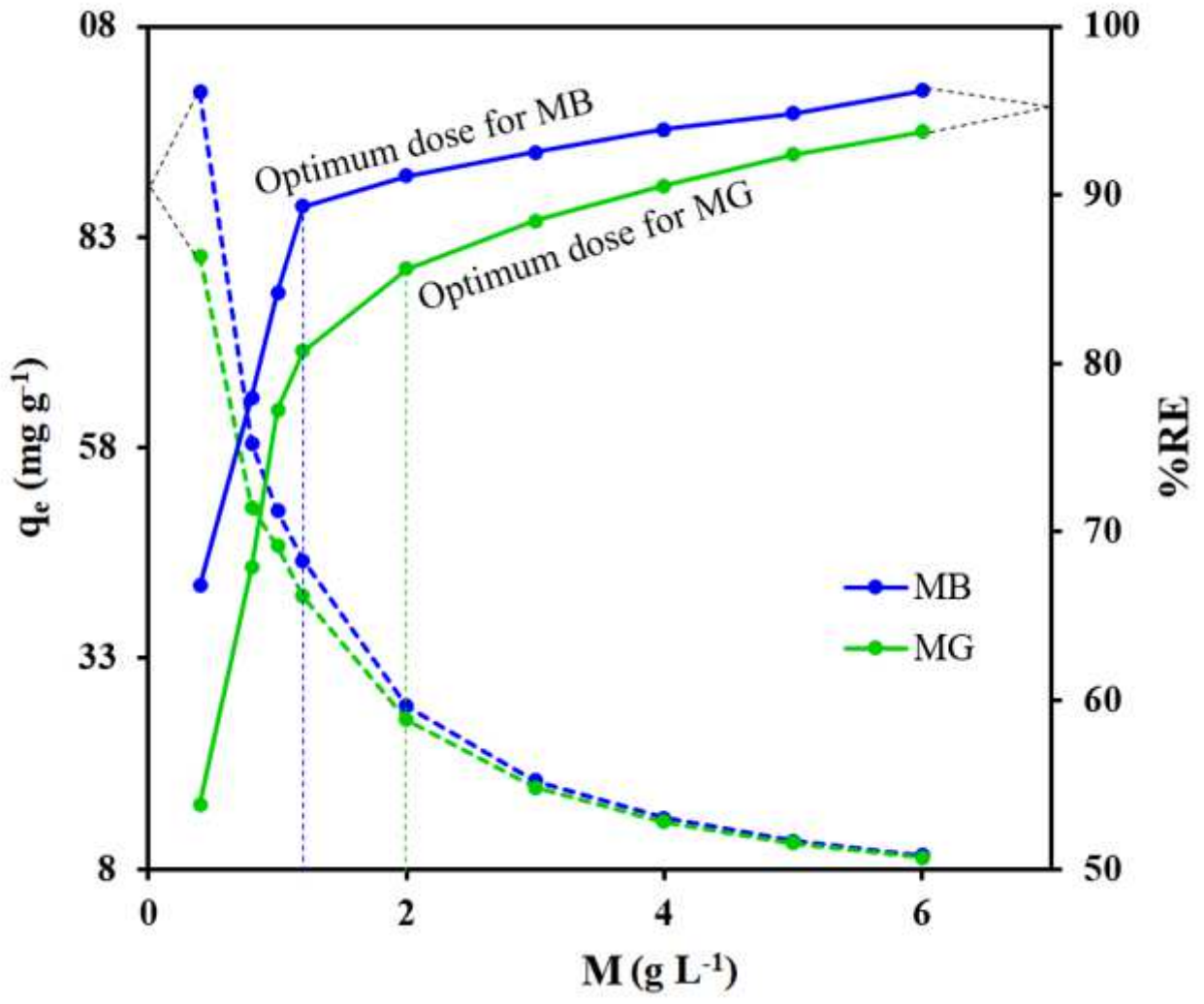


Figure 6

Effect of MChs dose on adsorption capacity (q_e) and removal efficiency (% RE) of MChi

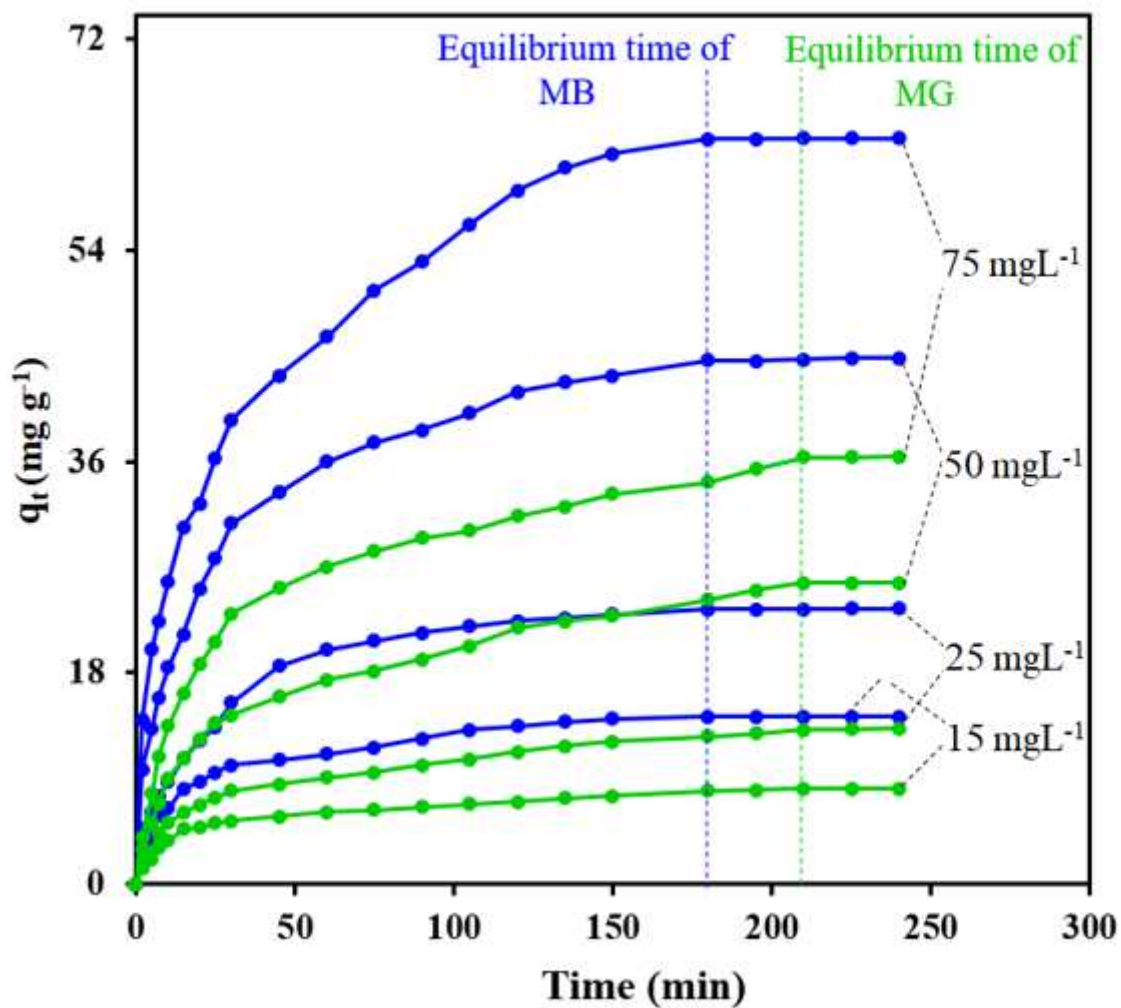


Figure 7

Effect of contact time on adsorption capacity of MChi

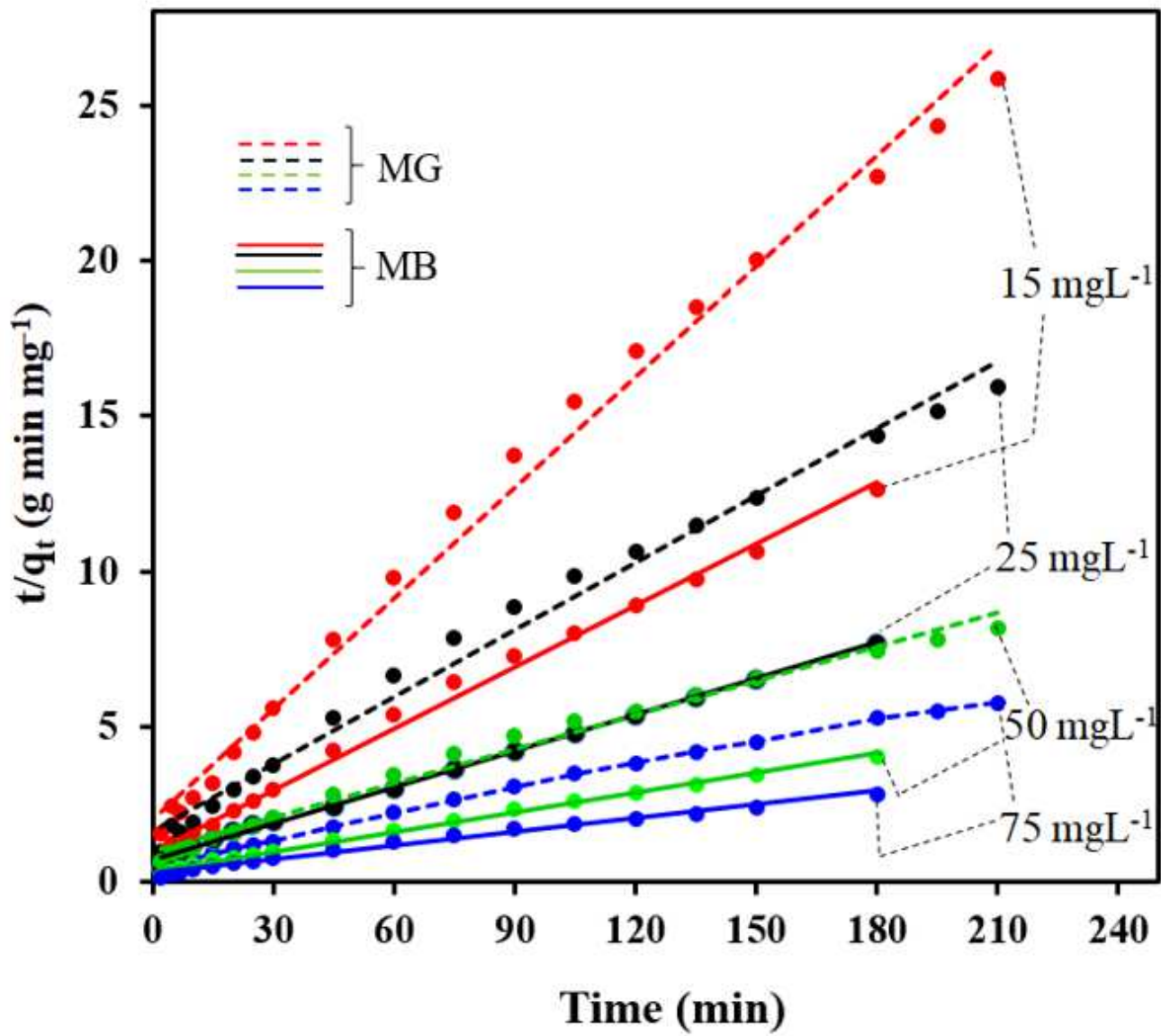


Figure 8

Pseudo-1st-order plot for the MG and MB adsorption onto the MChi

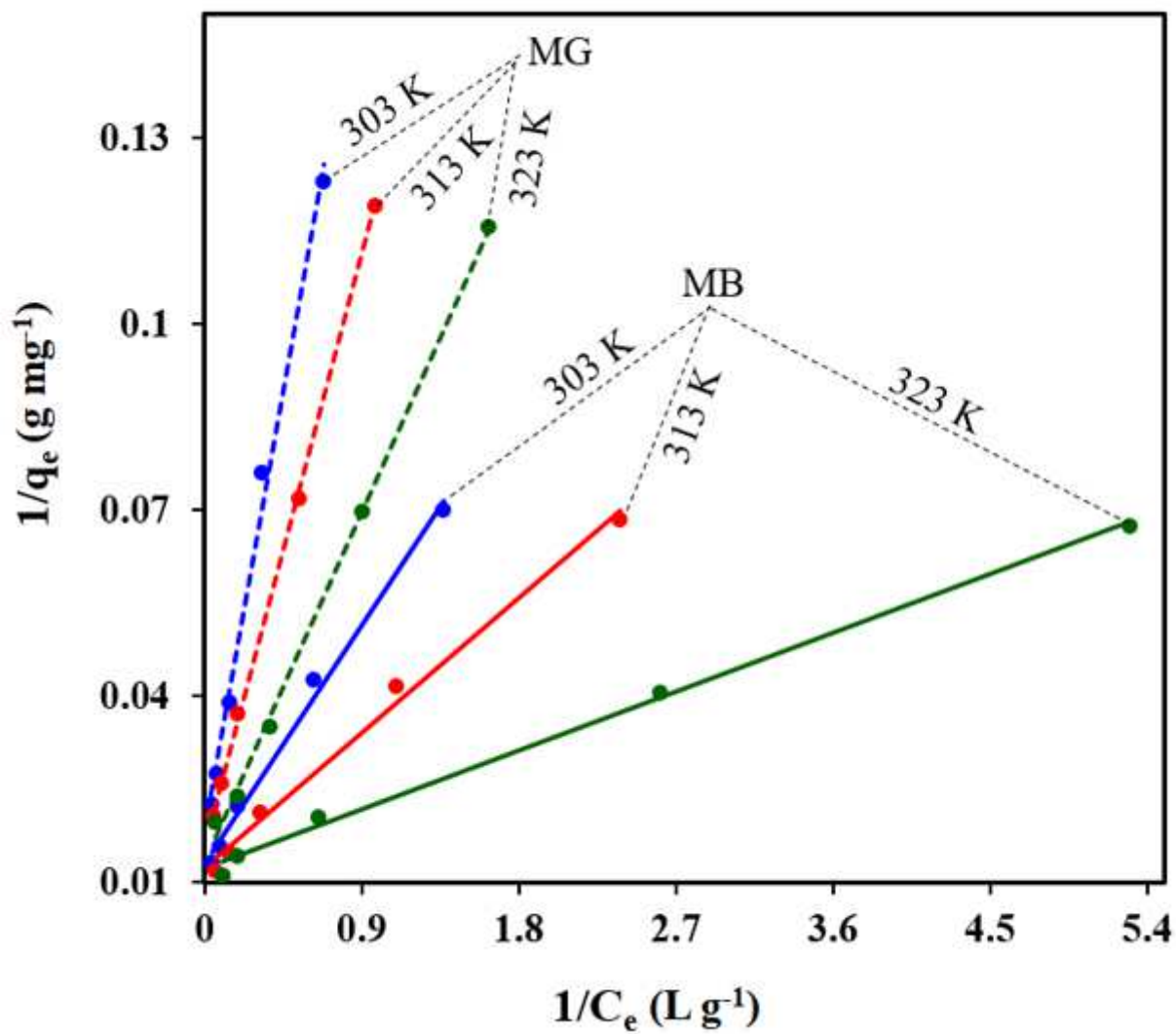


Figure 9

Langmuir model for the MG and MB adsorption onto the MChi

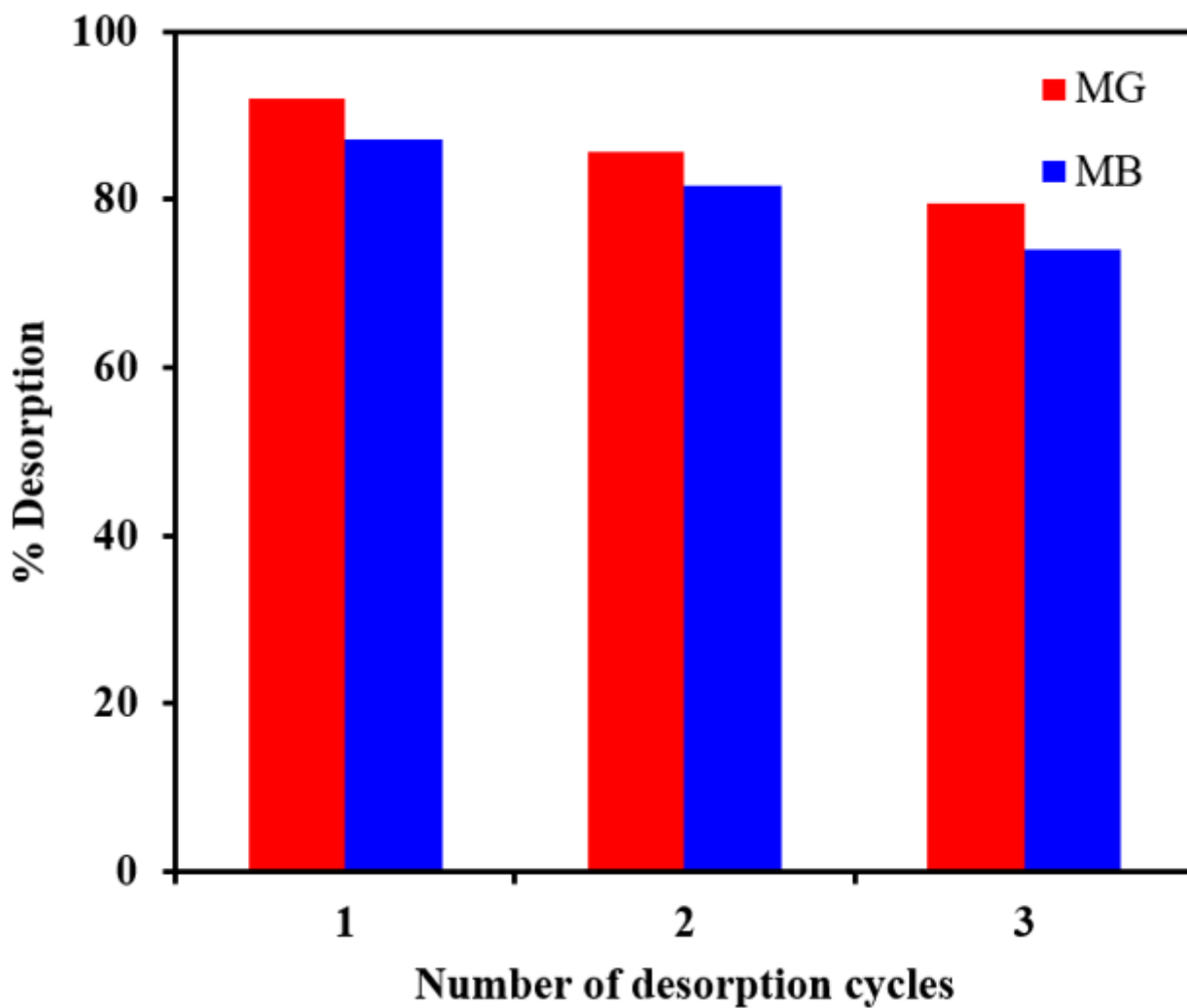


Figure 10

Reusability of MChi after adsorption of MG and MB

Supplementary Files

This is a list of supplementary files associated with this preprint. Click to download.

- [TextS1.docx](#)